Ahmad Kharrat

Master Thesis 2018 supervised by:
Univ.-Prof. Dipl.-Phys. Dr.habil. Holger Ott

Alkali-based Displacement Processes in Microfluidic Experiments: Advanced Statistical Analyses

dpe DEPARTMENT PETROLEUM ENGINEERING

MONTAN UNIVERSITÄT

To my lovely wife Negin and my beloved parents

Declaration

I hereby declare that except where specific reference is made to the work of others, the contents of this dissertation are original and have not been published elsewhere. This dissertation is the outcome of my own work using only cited literature.

Erklärung

Hiermit erkläre ich, dass der Inhalt dieser Dissertation, sofern nicht ausdrücklich auf die Arbeit Dritter Bezug genommen wird, ursprünglich ist und nicht an anderer Stelle veröffentlicht wurde. Diese Dissertation ist das Ergebnis meiner eigenen Arbeit mit nur zitierter Literatur.

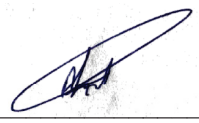

Name, 23 September 2018

Acknowledgements

I would first like to express my deep gratitude to my supervisor Prof. Holger Ott for his creative ideas, immense knowledge, thoughtful feedback and continuous support, which he has given me since the very beginning.

I would also like to thank my collogues Pit Arnold, Mostafa Borji, Neda Hassannayebi and Michael Koopmans for their guidance and support.

A loving thanks to my parents, especially my father, Prof. Riyaz Kharrat for unfailing supported, patience and continuous encouragement through my years of study.

To my wife Negin, thank you for your admirable love, rock-solid support and patience during my study.

Abstract

Since oil production declines over time, waterflooding and Enhanced Oil Recovery (EOR) are applied to increase the recovery, at the secondary and tertiary stages of production. Waterflooding is used for pressure maintenance and oil displacement, while the injection of chemically modified water may lead to a higher recovery in the tertiary stage of production. Water-based EOR methods, such as alkaline, surfactant and/or polymer flooding are commonly used due to their efficiency and low cost. Especially attractive is alkaline flooding, in which oil displacement is enhanced through interfacial tension (IFT) reduction, microemulsion generation and wettability alteration.

In this thesis, alkaline flooding was investigated by using microfluidics (2D porous media etched in glass) providing (a) a well-defined chemical environment and (b) displacements can be studied with high spatial and time resolutions. Hence, microfluidics allows studying chemical EOR processes in great detail.

In the frame of the present study, several experiments have been performed with different water compositions varying the alkalinity and salinity of the injection water. All the experiments were performed with crude oil of target field from Vienna basin, which has a high viscosity and TAN number. The flooding experiments have been performed in different porous media, representing high and low permeability and capillarity systems.

The purpose of this work was to enhance the experimental workflow in order to eliminate earlier observed inconsistencies. In this frame, it turned out that conventional measurements like the oil production from the porous medium (recovery) are not a good measurement, because the flooding domain does not represent an elementary volume for multi-phase flow.

Therefore, discrete frequency distribution and Lorenz plot analyses were applied to characterize the efficiency of water flooding and EOR process by acquiring quantities of data for comparing the results and understanding complex displacements.

Based on the obtained results, the synthetic water performed like an alkali agent and displaced a significant amount of oil compared to the pure-water flood. Upon statistical analyses, it has been observed that oil cluster size was reduced in alkaline flooding, which can be used as a fingerprint that distinguishes this process from water flooding. However, the link and

connection between statistical analyses with ultimate recovery were not achieved and still requires further investigation.

Zusammenfassung

Da die Menge an produziertem Öl mit der Zeit abnimmt, werden sekundäre und tertiäre Methoden, wie Wasserflutungen und Enhanced Oil Recovery (EOR), angewendet. Wasserflutungen werden zur Druckerhaltung und Verdrängung von Öl angewendet, wohingegen das Verpressen von chemisch modifiziertem Wasser im tertiären Stadium der Produktion zu einer höheren Ölgewinnung führt. Auf Wasser basierende EOR Methoden, wie Alkali-, Tensid- und/oder Polymerflutungen werden häufig verwendet, da sie kostengünstig und effizient sind. Besonders reizvoll sind dabei Alkaliflutungen, bei welchen die Menge an verdrängtem Öl durch die Reduzierung der Grenzflächenspannung, Bildung von Mikroemulsionen und Veränderung der Oberflächenbenetzung erhöht wird.

In dieser Arbeit wurden Alkaliflutungen mit Hilfe der Mikrofluidik (2D poröse Medien in Glas geätzt) untersucht, welche (a) eine chemisch gut definierte Umgebung liefern und (b) Verdrängungsprozesse können mit hoher räumlicher und zeitlicher Auflösung erforscht werden. Daher ermöglicht die Mikrofluidik die ausführliche Untersuchung chemischer EOR Prozesse.

Im Rahmen dieser Arbeit wurden mehrere Experimente mit Wässern unterschiedlicher Zusammensetzungen, welche sich in Alkalität und Salinität unterscheiden, durchgeführt. Alle Experimente wurden mit Rohöl vom Wiener Becken durchgeführt, welches eine hohe Viskosität und Gesamtsäurezahl hat. Die Flutungsexperimente wurden in verschiedenen porösen Medien, welche Systeme mit hoher und niedriger Durchlässigkeit und Kapillarität repräsentieren.

Das Ziel dieser Diplomarbeit war die Verbesserung der experimentellen Arbeitsabläufe um zuvor beobachtet Unbeständigkeiten beheben. In diesem Rahmen hat sich herausgestellt, dass konventionelle Messungen, wie die Öl Produktion von einem porösen Medium keine gute Messung ist, da der geflutete Bereich kein repräsentatives elementares Volumen für Mehrphasenströmung ist.

Daher wurden diskrete Häufigkeitsverteilungen und Lorenz Diagramm Analysen angewendet, um die Effizienz der Wasserflutungs- und EOR Prozesse durch Aneignung von Datenmengen

zum Vergleichen der Ergebnisse, sowie dem Verstehen der komplexen Verdrängungsprozesse, zu charakterisieren.

Aufbauend auf den erlangten Resultaten, verhält sich synthetisches Wasser wie ein Alkalimittel und verdrängt einen bedeutenden Anteil an Öl verglichen mit einer reinen Wasserflutung. Durch statistische Analysen wurde festgestellt, dass Ölgruppengrößen in alkalischen Flutungen reduziert wurden, was als Leitparameter zur Unterscheidung dieser Prozesse von Wasserflutungen genutzt werden kann. Jedoch konnte keine Verbindung zwischen den statistischen Analysen und der Gesamtproduktion von Öl hergestellt werden, weshalb noch weitere Untersuchungen vonnöten sind.

Table of Contents

List of Figures

List of Tables

Nomenclature

T	temperature	[c]
μ	Viscosity	[cp], [Pa.s]
σ	Interfacial tension	[mN/m]
Nc	Capillary number	[-]
u	Interstitial velocity	[m/s]
l^{cl}	Cluster length	[m]
V^{Darcy}	Darcy velocity	[m/s]
K^{rw}	Relative permeability of wetting phase	[-]
P^{c}	Capillary pressure	[Pa]
Q	Injection Flow rate	[microliter/h]

Abbreviations

EOR	Enhanced oil recovery
CDC	Capillary desaturation curve
IFT	Interfacial tension
WF	Water flooding
AF	Alkaline flooding
RF	Recovery factor
REV	Representative elementary volume

Chapter 1

Introduction

It is anticipated that the global energy demand will increase by around 35% from 2011 to 2035. Fossil fuels will be the focal source of energy and their share in the world's energy supply is expected to be around 80% in 2035 (International Energy Agency, 2013).

Hydrocarbon recovery operations consist of three phases. At first, oil is produced by natural depletion (primary recovery), while water or gas is generally injected subsequently (secondary recovery). If the reservoir is considered depleted by conventional means, enhanced oil recovery (EOR) techniques may be applied (tertiary recovery). Most oil reservoirs are candidates for enhanced oil recovery (EOR), while significant quantities of oil remain in place after applying traditional methods. Based on the published literature, there are many different EOR methods, which have been implemented and evaluated by the industry and academia. It is obvious that no single recovery method will apply to all reservoirs. Therefore, it is necessary to choose the best method for any given set of conditions, which is called EOR screening. EOR techniques are increasingly being considered to satisfy the growing demand of oil in future. In fact, it has been suggested that 88 billion barrels of oil will produce additionally, by increasing 1% of oil recovery factor, at current rates (Sheng, 2013). Chemical flooding may be applied in tertiary oil recovery by adding polymers, alkaline, and surfactants to the injection water, which helps the mobilization of the trapped oil in the reservoir rock by decreasing the interfacial tension, by altering wettability, and by enhancing water viscosity (S. Kokal, 2010). This could be achieved through single or multiple changes in reservoir fluids properties and its interfacial energy (Lake, 1989). Alkaline flooding is one of the earliest-applied and cheapest methods amongst chemical flooding methods. The primary mechanisms are the reduction of interfacial tension, the resulting microemulsion generation and a change in wettability.

In the frame of this thesis, alkaline flooding is investigated by using microfluidics (2D porous media etched in glass)

1.1 Background and Context

Alkaline flooding was first performed in the 20th century. However, few works have been reported in alkaline flooding recently. (Borji, 2017) and (Arnold, 2018) achieved significant results on alkaline flooding on the pore scale using microfluidics and on fluid-fluid interfacial properties, respectively. The present thesis is following the earlier work and applied similar techniques to obtain a better understanding of the processes by investigating their fingerprints.

1.2 Scope and Objectives

In this work, fluid displacements are investigated on the pore scale for different injection-water solutions with different alkalinity. Furthermore, displacements have been studied in two different microfluidic devices, representing low and high capillarity systems.

One of the objectives is to achieve repeatable and reproducible results in the experiments. Moreover, by applying statistical analyses, we found quantitative signatures of water and alkaline flooding processes, and a relationship between statistical analyses and ultimate recovery factor.

Chapter 2

Literature Review

This chapter describes the basic principle and gives a brief introduction to oil recovery and their mechanism on the macroscopic and microscopic scale.

2.1 Oil recovery and EOR

The hydrocarbon production from underground history dates back to the 18th century. From then, different operations were used to increase the hydrocarbon recovery, which is divided into primary, secondary, tertiary (EOR) recovery methods. Upon the increase of the oil price, EOR becomes more demanding, while the recovered oil form most of the reservoirs is less than 50 % without EOR. There is a different type of EOR classification methods such as conventional and unconventional (Riyaz Kharrat, 2017) or chemical, thermal, solvent and other (Larry W. Lake, 2014). The main mechanism of chemical EOR is to increase the capillary number to mobilize remaining oil and to control the mobility to increase the sweep efficiency (Hu Guo, Ma Dou, Wang Hanqing, Fuyong Wang, Gu Yuanyuan, Zhaoyan Yu, Wang Yansheng, Yiqiang Li, 2017). The main focus of this thesis is on alkaline flooding.

2.2 Alkaline Flooding

In 1917 Squires, the first-time added alkali to the injection water, and observed that oil displacement improved (Squires, 1917). This method is one of the cheapest, which is still used (E.F. deZabala, 1982). Based on the literature, Alkaline flooding has been used in 36 projects and six different countries (Sheng, 2015).

2.2.1 Alkaline reaction with oil

The reaction between an acid component of the oil and alkali agents leads to soap generation at the oil and water interface (C. E. Cooke, 1974). Figure 2-1 shows a schematic view of this process.

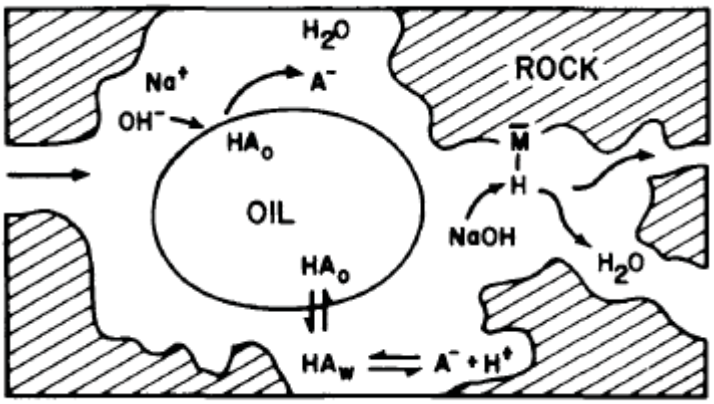

Figure 2-1- Schematic picture of alkali process (E.F. deZabala, 1982)

To understand the saponification, a number of chemical reactions need to be considered. The dissociation reaction of sodium hydroxide in water is shown in equation (2-1) and the reaction of sodium hydroxide with an acid oil component is illustrated in Equation (2-2), where HA represents the acid component of oil.

$$NaOH \rightarrow Na^+ + OH^- \quad (2\text{-}1)$$

$$HA + Na^+ + OH^- \Leftrightarrow NaA + H_2O \quad (2\text{-}2)$$

Equation (2-3) and (2-4) show the sodium carbonate dissociation and formation of carbonic acid. Additionally, equation (2-5) describes the reaction of oil acid component.

$$Na_2CO_3 \rightarrow 2Na^+ + CO_3^{2-} \quad (2\text{-}3)$$

$$H_2O + CO_3^{2-} \rightarrow H_2CO_3 + OH^- \quad (2\text{-}4)$$

$$HA + OH^- \rightarrow A^- + H_2O \quad (2\text{-}5)$$

Both alkali agents were used in this thesis.

Alkaline flooding performance is mainly depending on crude oil and water composition, rock reactivity and alkaline concentration and slug size (Johnson, 1976). Up to this point, eight different mechanisms are known for this EOR method, which are shown in the following (E.F. deZabala, 1982):

- Emulsification with entrainment
- Emulsification with entrapment
- Emulsification with coalescence
- Wettability reversal
- Wettability gradients
- Oil-phase swelling
- Disruption of rigid films
- Reducing interfacial tensions

Some of these mechanisms have been observed by Borji (Borji, 2017) and in the frame of this thesis.

- **Reduction of IFT**

In alkaline flooding, the IFT reduction results from the in-situ generated soap which is forming of reaction between an acid oil and an alkali solution (C. E. Cooke Jr., R. E. Williams, P. A. Kolodzie, 1974). Moreover, Capillary force is also decreased as a result of IFT reduction, which is discussed further below in the context of the Capillary Desaturation curve.

- **Emulsification**

If the IFT reduced significantly, the mixture of oil and water may lead to emulsion formation. Emulsification is mainly divided to entrainment and entrapment

Emulsification and entrainment

The oil emulsifies in water due to IFT reduction and displaced within the aqueous phase (Subkow, 1942). Therefore, the displacement efficiency improved which leads to higher oil recovery.

Emulsification and entrapment

If the size of emulsified oil clusters is larger than the pore throat sizes, the flowing paths will block by the emulsion. Therefore, the fluid flows through unswept pores and the sweep efficiency increases. However, this mechanism is only observed in heavy viscous oil with a high TAN number (Ehrlich R., Hasiba H.H., Raimondi P., 1974).

- **Wettability reversal**

Depend on the initial condition, the change from oil-wet to water-wet may occur or the reverse. When an oil-wet system changed to a water-wet, the relative permeabilities also change in favourable direction and leads to oil recovery improvement. Thought, changing the water-wet to oil-wet reservoir results to connecting the discontinuous residual oil phases and providing the flow path for trapped oil. Additionally, oil-external emulsions of water droplets block the flow and induce a high-pressure gradient, which can overcome the capillary force (Sheng, 2011).

2.3 Capillary Desaturation curve

To describe the impact of alkaline flooding on residual oil in the reservoir the capillary desaturation curve (CDC) is used. CDC is one of the fundamental concepts in enhanced oil recovery and describes the relationship between residual saturation of wetting and non-wetting fluid phase with the capillary number (N_c). This number is the ratio of viscous forces to capillary forces and is defined in equation (2-6), where μ and u are the viscosity and interstitial velocity of the displacing fluid or wetting phase, respectively, and σ is the interfacial tension between two fluids (Larry W. Lake, 2014). The nonwetting saturation is constant at plateau value, when the capillary number is small. The reduction of nonwetting saturation starts at critical capillary number. This number is achieved either by increasing the viscous force or reducing the capillary force.

$$N_c = \frac{Viscous\ force}{Capilarry\ force} = \frac{\mu u}{\sigma} \tag{2-6}$$

Figure 2-2 shows a schematic CDC, where the X-axis denotes the capillary number and Y-axis denotes the residual nonwetting or wetting residual phase saturation. The critical capillary number, above which desaturation occurs is about Nc ~ 10^{-5} to 10^{-7} depending on the wetting state of the sample (Dullien, 1979).

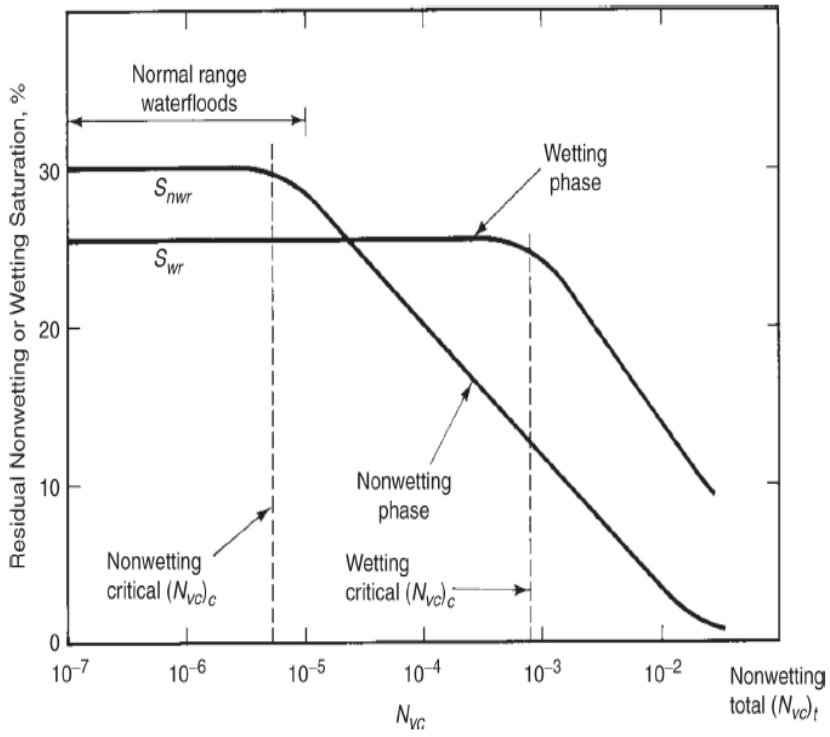

Figure 2-2- Schematic CDC (Larry W. Lake, 2014)

In 1974, Melrose and brander proposed new capillary number (macro capillary number) by applying the Darcy law into the equation. They stated that by achieving the IFT value in the order of 10^{-3} to 10^{-4} dynes/cm, the residual oil saturation would be reduced (J. C. Melrose, C. F. Brandner, 1974). Later on, Hilfer and Øren (A. Lucian, R. Hilfer, 1999) proposed a new equation for macro capillary number based on connecting and upscaling the microscopic and macroscopic images. In 2014, Armstrong, Georgiadis, and Ott modified the Lucian and Hilfer model and defined a new equation (2-7), where l^{cl} is the cluster length in the flow direction, μ^w is wetting phase viscosity, V^{Darcy} is Darcy velocity, K^{rw} is relative permeability of wetting phase and P^c is capillary pressure. The average value of these parameters is measured from the X-ray computed microtomography and transformed from micro (pore scale) to macro scale. Moreover, they observed the nonwetting phase mobilization at $N_c^{macro} \sim 1$ (Ryan T. Armstrong, Apostolos Georgiadis, Holger Ott, Denis Klemin, Steffen Berg, 2014)

$$N_c^{macro} = \frac{l^{cl}\mu^w V^{Darcy}}{K^{rw}P^c} \tag{2-7}$$

Yegane and Hegner simplified the capillary number by applying the flow rate and Darcy law in the equation and proposed that the critical oil ganglia lengths have an inverse relation with the capillary number and it depends on rock properties such as porosity and permeability. (Mohsen Yeganeh, Jessica Hegner, Eric Lewandowski, Aruna Mohan, Larry W. Lake, Dan

Cherney, Arben Jusufi, Aditya Jaishankar , 2016). Equation (2-8) shows the capillary number, where the Q is the flow rate, A is the area and ϕ is the porosity.

$$N_c^{micro} = \frac{\mu^w Q}{A \partial \phi} \tag{2-8}$$

2.4 Microfluidics

The displacement processes can be studied with high spatial and time resolutions in microfluidics devices. Micromodels are simplified porous network, which may represent a rock structure, or any other porous medium. It is essentially a 2D pore structure etched in glass (in this thesis), with the structure being covered by another glass plate. Microfluidic experiments were first performed by Chatenever and Calhoun in 1952. Their model was developed to study fluid flow in porous media (A. Chatenever, J. Calhoun, 1952). Later, the cover glass was etched chemically with hydrofluoric acid in order to create networks (C. Mattax, J.R. Kyte, 1962). Since then, microfluidics has extensively been used to study two-phase flow and displacement mechanisms. A famous example is the study by Lenormand investigating displacement stability and the structure of the resulting displacement patterns (Roland Lenormand, Cesar Zarcone, 1985)

Micromodels are manufactured from transparent materials such as glass or polymer-based materials, which are cheaper compared to glass (Shao-Yiu Hsu, Zhong-Yao Zhang, Chia-Wen Tsao, 2017). Nowadays, the complex porous media can be manufactured with a high degree of details by using laser technology (N. K. Karadimitriou and S. M. Hassanizadeh, 2012).

The use of microfluidics is well established to examine the microscopic behavior of multiphase flow in porous media. It gives a significant advantage to see the movement of fluid interfaces and makes it possible to distinguish between different kinds of mechanisms that may all lead to similar production behavior. The size and depth of the pore structure are adjustable and may serve different objectives of the experiment. Figure 2-3 shows a pore structure with a rather random distribution of grains as it has been used in this thesis. The white color describes the pore space and flowing path, while the grains are shown with black color in the micromodel. The dimensions of the porous domain are 2 cm in length, 1 cm width and 20 microns etching depth.

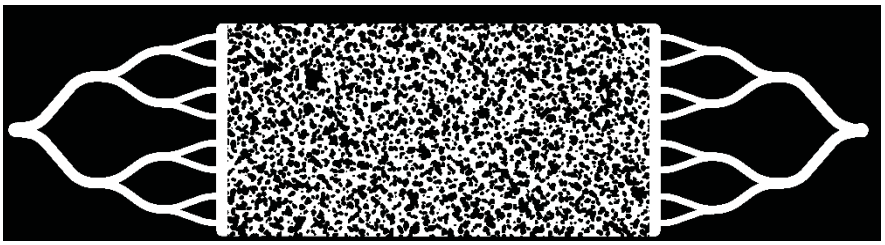

Figure 2-3- Micromodel from Micronit company, white color shows the flowing channels

2.5 Displacement process in pore scale

Two phase immiscible displacements are a complex process and especially rich on the pore scale. This can best be illustrated by the work of Lenormand; he observed several fundamentally different displacement patterns on the pore-scale. The displacements could be characterized by viscous and capillary fingering and stable displacement as a function of the mobility and capillary number (R. Lenormand, 1990). It should be mentioned that mobility number was defined as the ratio of viscosity of the displacing fluid to the displaced fluid. Moreover, viscous fingering occurs mainly when the displacing fluid has a lower viscosity compared to the displaced fluid. The invasion-percolation theory describes the capillary fingering, where the fluids flow in pore throats will lower capillary forces (Christophe Cottin, Hugues Bodiguel, Annie Colin, 2010). Additionally, the stable displacement achieved by increasing the viscous forces. This also is shown as phase diagram in Figure 2-4. The graph is double log scale, where X-axis is logarithm of mobility number (Ratio of displacing fluid to displaced fluid) and Y-axis is logarithm of capillary number (Y. Alzahid, P. MOstaghimi, M. Ebrahimi Warkiani, R T. Armstrong, 2017).

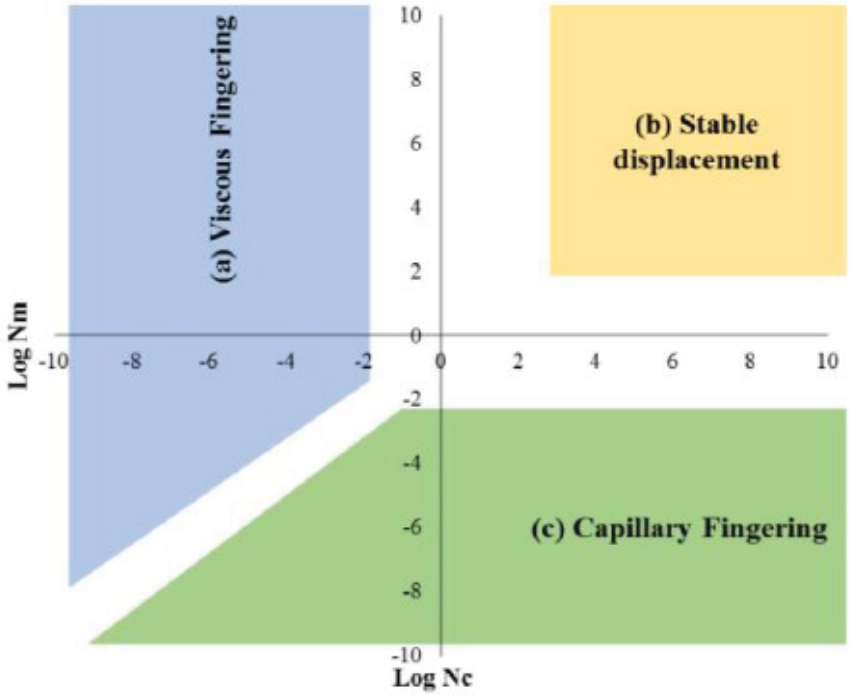

Figure 2-4- Phase diagram of displacement patterns (Y. Alzahid, P. MOstaghimi, M. Ebrahimi Warkiani, R T. Armstrong, 2017)

In term of capillary and mobility number, the stable displacement occurs, where the mobility and capillary numbers are close to one. While viscous fingering is occurring with high mobility and low capillary numbers. In contrast, the capillary fingering occurs with low mobility and high capillary numbers. The experimental observation of the displacement and transition and crossover zone between these displacements are shown in Figure 2-5. The blue color illustrated the transition zone between capillary to viscous fingering. The experimental observation is shown in Figure 2-6, where ‘y’, ‘z’, ‘z1’ and ‘z2’ demonstrate the capillary fingering and ‘a-d’ illustrate viscous fingering displacement. Additionally, ‘cz’ shows the transition zone between these two displacement processes (Yi-Feng Chen, Shu Fang, Dong-Sheng Wu, Ran Hu, 2017).

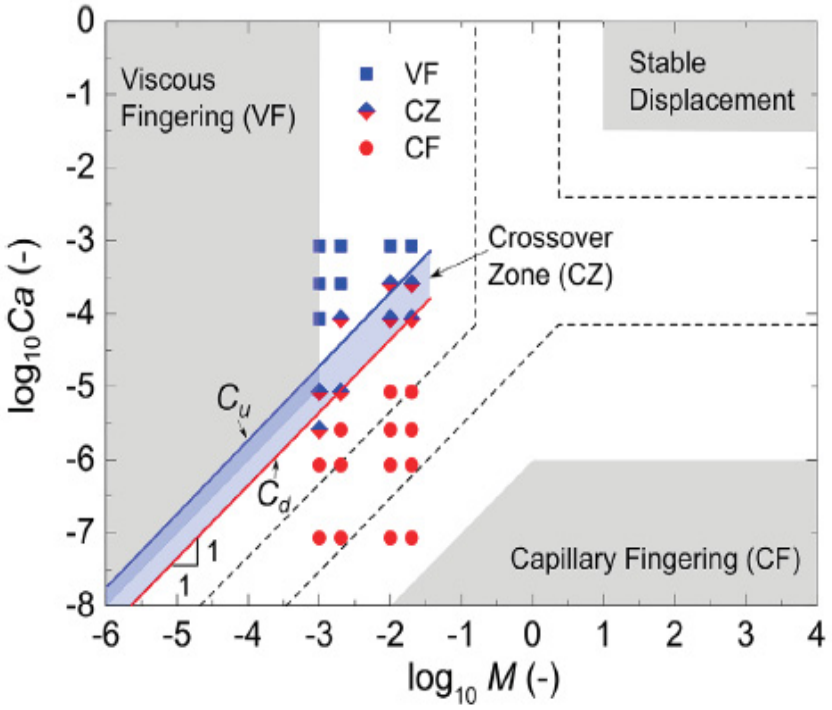

Figure 2-5- Displacement patterns and the transition zone between them (Yi-Feng Chen, Shu Fang, Dong-Sheng Wu, Ran Hu, 2017)

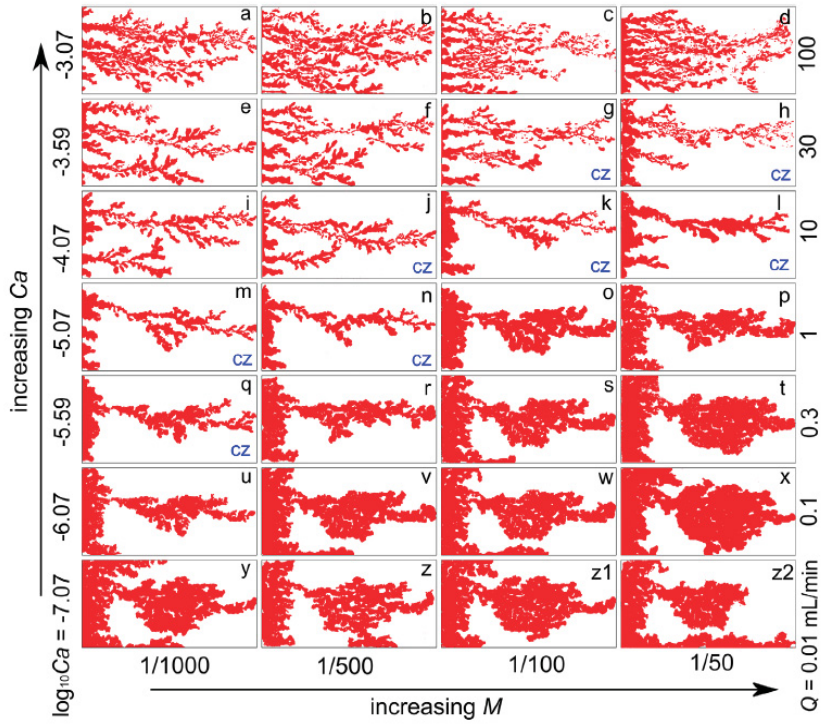

Figure 2-6- Displacement patterns observation based on capillary and mobility number in fractured micromodel (Yi-Feng Chen, Shu Fang, Dong-Sheng Wu, Ran Hu, 2017)

Chapter 3

Experimental Equipment

In this chapter, the experimental equipment used in this thesis will be discussed. The setup has been assembled and commissioned in the frame of the thesis. Different options with respect to image stitching, cameras for particle tracing etc. were tested and the setup respectively extended. The overall setup is shown in Figure 3-1.

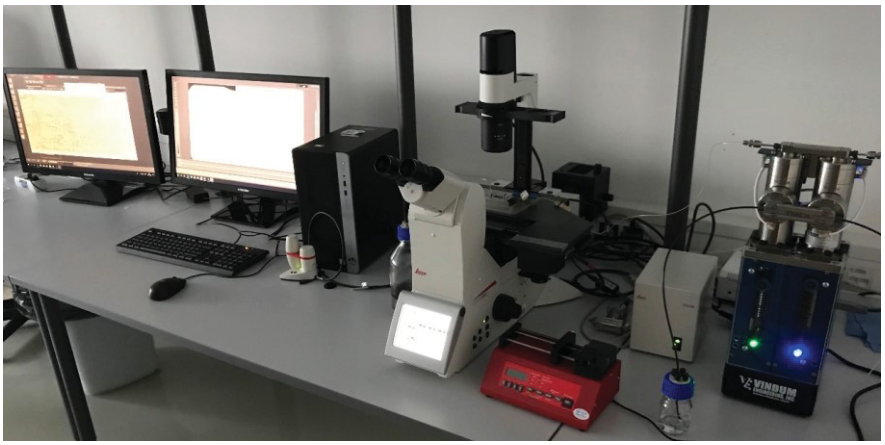

Figure 3-1- Experiment setup

3.1 Injection and Vacuum material

Two different pumps were used in the experiments. A conventional syringe pump was used for pre-saturating the micromodel with oil, while a high-precision dual piston pump was employed for the actual time-resolved injection experiments. In addition, the vacuum pump is utilized to remove the air from the system prior to the initial saturation step.

Syringe pump

Syringe pumps are used in most of the laboratory as economical equipment. In this thesis, NE 300 syringe pump from ProSense company was used, which is shown in Figure 3-2.

Figure 3-2- NE-300 syringe pump

Syringes are utilized for cleaning purpose and oil injection. The crude oil contains particles, which could settle down in the piston pump. Therefore, using syringes and syringe pumps are more practical. 10 ml Lure lock form B. Braun company with 15.9 mm inner diameter (Figure 3-3- right) as a plastic syringe and 5 ml tight gas glass syringe from Hamilton company with 10.3 mm inner diameter (Figure 3-3- left) were conducted. The glass syringe is used for cleaning while the plastic syringe reacts with cleaning agents.

Figure 3-3- Syringe (Left, glass syringe, right- Plastic syringe)

Piston pump

For the time-resolved flooding experiments, i.e. the water injection, a more accurate pump was required. A high-precision pulse-free dual piston pump from Vindum Engineering (Figure 3-4) was used for that purpose. This kind of pump injects pulse-free continuous fluid flow which results in high accuracy in the injection rate and result.

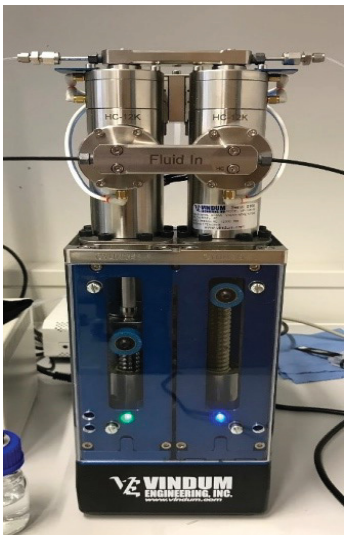

Figure 3-4- Vindum VP-12K continuous pulse-free high-pressure metering pump

In addition, the vacuum pump was utilized to remove the air from micromodel in the last step of the cleaning process. Welch MPC 301 Z vacuum pump was conducted in this work, which is shown in Figure 3-5. The time for evacuation the air from the system was approximately 5 hours.

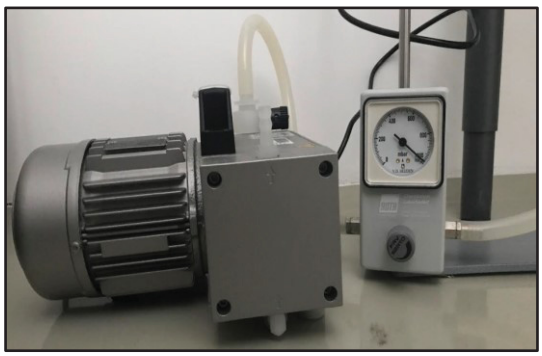

Figure 3-5- Vacuum pump

3.2 Micromodel and Chip holder

Physical-rock-pattern and uniform-network micromodels from the company Micronit has been used as porous media throughout this thesis. The micromodels were mounted in a high-pressure chip holder from the same company (Figure 3-6). The physical rock pattern has a rather irregular structure, representing a low-capillarity system, while the uniform pattern shows a quite regular and rather narrow structure leading to higher capillarity. The more detailed information is shown in Table 3-1.

Table 3-1- Micromodels specification (Micronit, 2018)

	Physical rock micromodel	Uniform micromodel
size	45 mm x 15 mm	45 mm x 15 mm
Channel height	20 µm	20 µm
Rockpore volume	2.3 µl	2.1 µl
Porosity	0.57	0.52
Permeability	2.5 Darcy	2.5 Darcy

Figure 3-6- Physical rock micromodel in left and High-Pressure chip holder in right (Micronit, 2018)

3.3 The Microscope

The images have been taken with a Leica DMi 8 high-end microscope as shown in Figure 3-7. This model is an inverted light microscope with space for five different objectives. In these experiments, objectives with 2.5X and 5X magnification are applied. In addition, the microscope has a fluorescence option, which has been tested in the frame of the thesis. The field of view is based on the magnification and is shown in Table 3-2. The images are taken with a Leica DMC2900 camera, which is connected to the computer, and an objective with 0.7X c-mount to improve the stitching quality. In addition, it is possible, to acquire an image of the entire flooding domain with an automatic stitching option. Las X software from Leica company has been used for image acquisition.

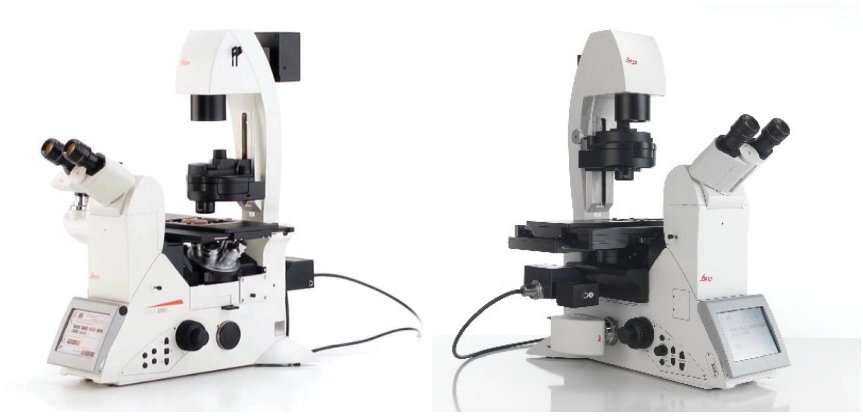

Figure 3-7- DMi 8 Leica microscope (www.leica-microsystems.com)

Table 3-2- Field of view for microscope objectives

Magnification	Field of view (micrometer)
2.5X	3742 x 2806
5X	1871.09 x 1403.09
10X	935 x 701.54
20X	467 x 350

Chapter 4

Experimental methodology

This chapter describes the overall workflow including the experiments, the image analysis and the statistical analysis on basis of the images. In addition, detail of all performed experiment is given.

4.1 Alkaline Flooding Methodology

In all the experiments, fluids were injected in micromodels in the same orientation. In the following images, this will consistently be from right to left. Two different injection rates (0.01 ml/h and 0.001 ml/h) were used. The experiments were performed at room temperature and it should be mentioned that it was not possible to control the room temperature to which we refer some of the inconsistencies in the experimental results.

4.1.1 Cleaning the micromodel

The cleaning method was performed following (Borji, 2017). The first step is to inject 50 pore volume of acetone. Afterward, 50 pore volume toluene is injected for several hours until no further oil was visible in the flooding domain and in the injection lines. For cleaning the toluene from the microchip, acetone is injected as in the first step. The final step is air injection to vaporize the acetone and then until no liquid is in the system. Finally, vacuum is applied to remove the air from the system. The cleaned micromodel is shown in Figure 4-1.

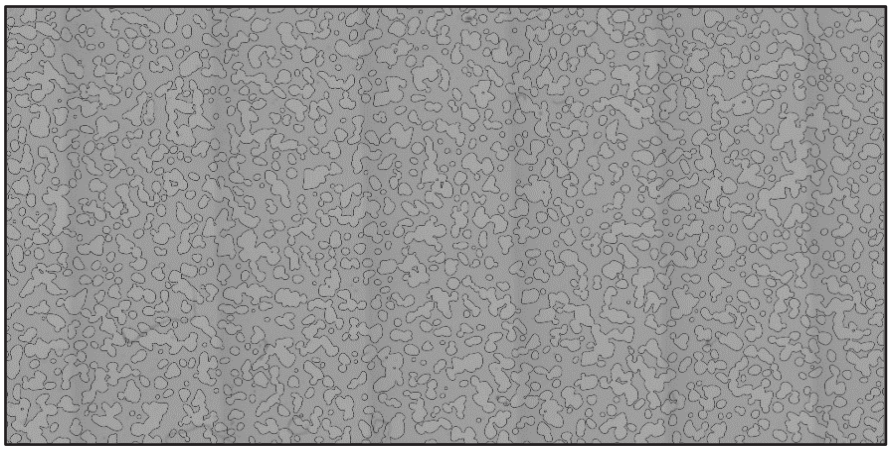

Figure 4-1- Cleaned micromodel

4.1.2 Saturating micromodel with oil

After cleaning, oil was injected under vacuum conditions using the syringe pump until the micromodel was saturated 100% with oil. The result of this pre-saturation step is shown in Figure 4-2.

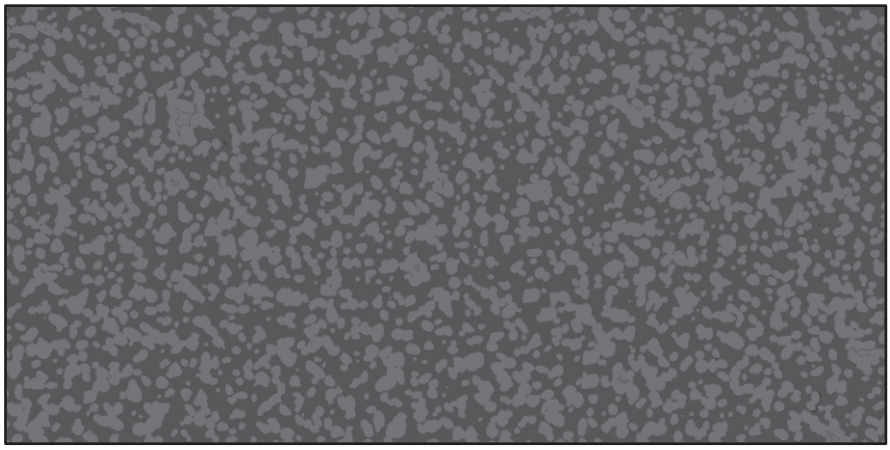

Figure 4-2- 100% oil-saturated micromodel

4.1.3 Water flooding

To simulate water flooding, water has been injected using the high-precision displacement pump delivering a high accuracy flow rate through the oil saturated micromodel. The injected water is displacing the oil from the porous medium in characteristic ways. Distilled and synthetic water (distilled water + 22.09 g/l NaCl + 1.5 g/l $NaHCO_3$) with salinity around 23500 ppm were injected. The injection was continued, until no further displacement in the micromodel was obtained. The total flooding time was approximately 22 hours for the 0.01 ml/h flow rate. Figure 4-3 shows the distilled water flooding after 22 hours.

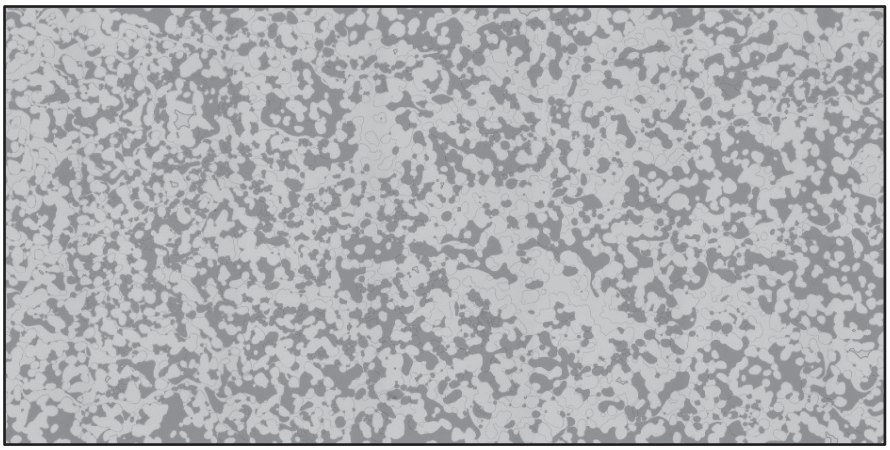

Figure 4-3- Micromodel after water flooding, dark areas correspond to remaining oil at the end of the water flood

4.1.4 Alkaline flooding

Subsequently, an alkaline solution was injected in the same way as for the water injection. The duration for all alkaline flooding was not exceeding 24 hours.

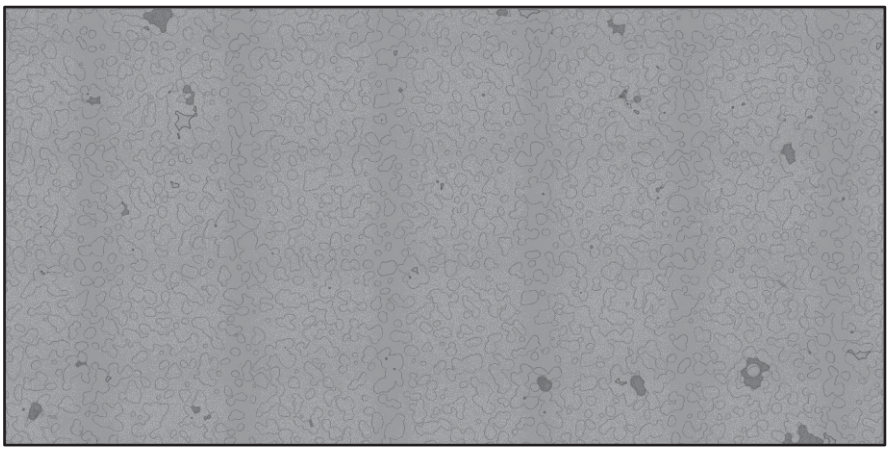

Figure 4-4- The final stage of alkaline flooding (Sodium hydroxide), dark areas correspond to remaining oil at the end of the alkaline flooding.

4.1.5 IFT measurement

The IFT values at 25°C are taken from (Arnold, 2018) and are shown in Table 4-1. It should be noted that in some of the measurement such as 7500 ppm sodium carbonate with distilled water, 3 phase systems (Oil, water, Microemulsion) were observed, where microemulsion phases were generated and separated from the oil component. This behavior has earlier been observed and

may lead to an increase in IFT (Arnold, 2018). The following IFTs have need measured for the relevant oil/water combinations (Arnold, 2018):

Table 4-1- IFT measurement at 25°C (Arnold, 2018)

Oil	Fluids	IFT [mN/m]
Crude oil 8th	Distilled Water	0.35
Crude oil 8th	Synthetic Water	0.032
Crude oil 8th	950 ppm Na_2CO_3 with distilled water	0.07
Crude oil 8th	3000 ppm Na_2CO_3 with distilled water	0.065
Crude oil 8th	3000 ppm Na_2CO_3 with Synthetic Water	0.15
Crude oil 8th	6000 ppm Na_2CO_3 with distilled water	0.07
Crude oil 8th	7500 ppm Na_2CO_3 with distilled water	0.065
Crude oil 8th	7500 ppm Na_2CO_3 with Synthetic Water	0.3

4.1.6 Experiments details

Several experiments were performed in the frame of this thesis, which are listed in Table 4-2.

Table 4-2- Experiments details

Experiment	Water flooding	Alkaline flooding	Injection rate [ml/h]	Micromodel
Experiment 1.1	Distilled water		0.01	Physical rock
Experiment 1.1.1		3000 ppm Na_2CO_3 with distilled water	0.01	Physical rock
Experiment 2.1	Distilled water		0.01	Physical rock
Experiment 2.1.1		3000 ppm Na_2CO_3 with distilled water	0.01	Physical rock
Experiment 3.1	Distilled water		0.01	Physical rock
Experiment 3.1.1		7500 ppm Na_2CO_3 with distilled water	0.01	Physical rock
Experiment 4.1	Distilled water		0.01	Physical rock
Experiment 4.1.1		7500 ppm Na_2CO_3 with distilled water	0.01	Physical rock
Experiment 5.1	Synthetic water		0.01	Physical rock
Experiment 5.1.1		3000 ppm Na_2CO_3 with synthetic water	0.01	Physical rock
Experiment 6.1	Synthetic water		0.01	Physical rock
Experiment 6.1.1		7500 ppm Na_2CO_3 with synthetic water	0.01	Physical rock
Experiment 7.1	Distilled water		0.01	Physical rock
Experiment 7.1.1		720 ppm NaOH with distilled water	0.01	Physical rock
Experiment 8.1	Distilled water		0.01	Physical rock
Experiment 9.1	Distilled water		0.001	Physical rock
Experiment 9.1.1		720 ppm NaOH with distilled water	0.001	Physical rock
Experiment 10.1	Distilled water		0.001	Regular
Experiment 10.1.1		720 ppm NaOH with distilled water	0.001	Regular
Experiment 11.1	Distilled water		0.001	Regular
Experiment 11.1.1		950 ppm Na_2CO_3 with distilled water	0.001	Regular
Experiment 12.1	Distilled water		0.001	Physical rock
Experiment 12.1.1		6000 ppm Na_2CO_3 with distilled water	0.001	Physical rock
Experiment 13.1	Distilled water		0.001	Regular
Experiment 13.1.1		6000 ppm Na_2CO_3 with distilled water	0.001	Regular

4.2 Image Acquisition

The Leica Dmi8 microscope is able to move the acquisition stage automatically. Two diagonally opposite locations of the micromodel are marked as scanning range to obtain a complete view. The software will divide the selected area into smaller parts. Afterward, the stage moves automatically and the camera will capture the induvial picture from each section,

which will be merge and stitch after the final image is taken. Time resolution of 35 seconds can be reached for imaging the total porous domain. In this thesis, for physical rock pattern, 2.5X magnification was used which results in 34 tile images (Figure 4-5-a), while the uniform pattern requires 5X magnification and 108 tile images (Figure 4-5-b).

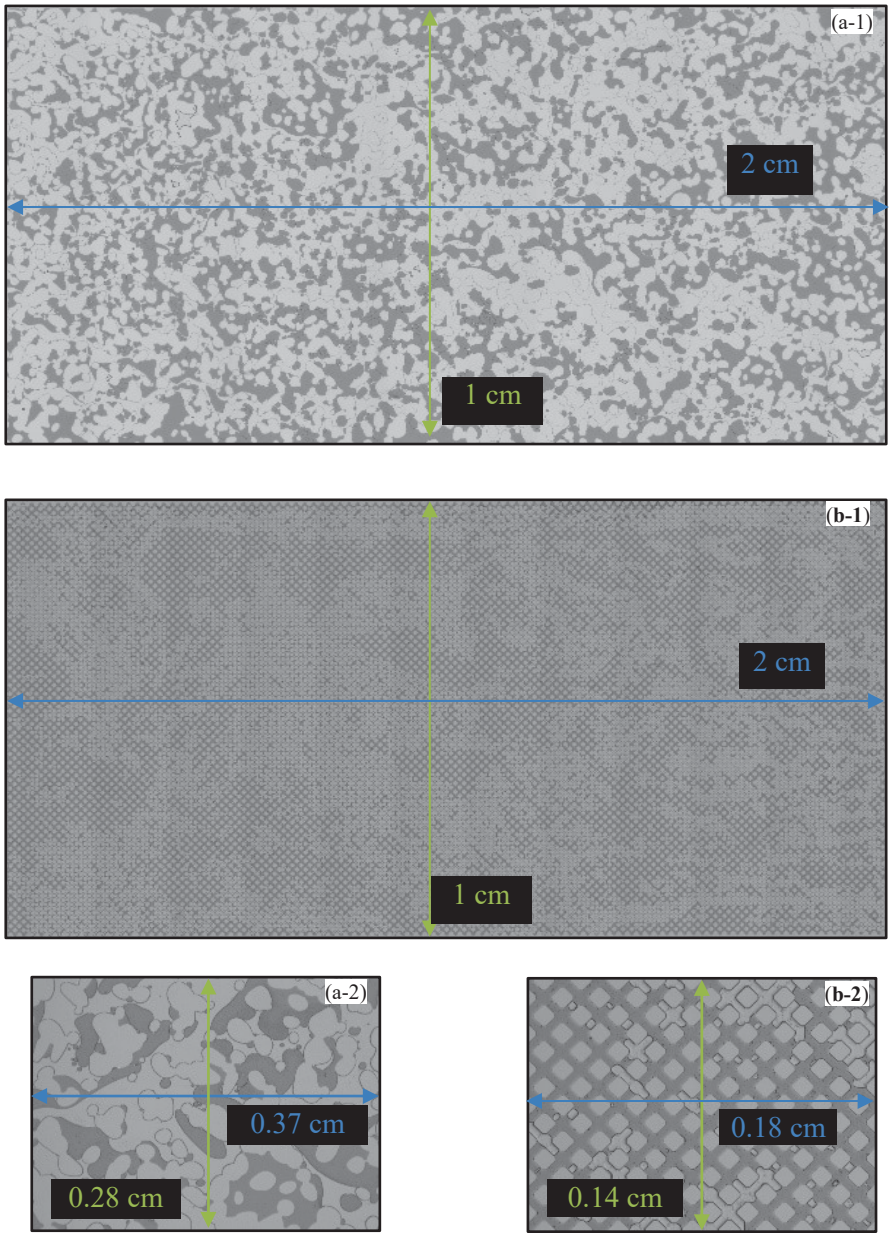

Figure 4-5- Individual (lower row) and stitched images for a) the physical rock pattern, and b) the uniform pattern.

4.3 Image Analyses

Images consist of pixels with a gray-scale assigned to each pixel. The objective of the image analysis is to identify the individual fluid phases, i.e. to discriminate water form oil and form the “obstacle, respectively the rock grains”. This requires optical contrast between the phases, which can be used to binarize the images in grains, and oil phase and an aqueous phase. Therefore, the first step in the image processing is to binarize the picture and converting the value to zero and one this is called image segmentation. Figure 4-6-a shows a raw picture of empty physical rock micromodel with values between 0 and 255. The binarized image is shown in Figure 4-6-b, which has only two values, 0 and 255 or black.

ImageJ (develop by Contributors worldwide) is applied to the image analyzing in this thesis.

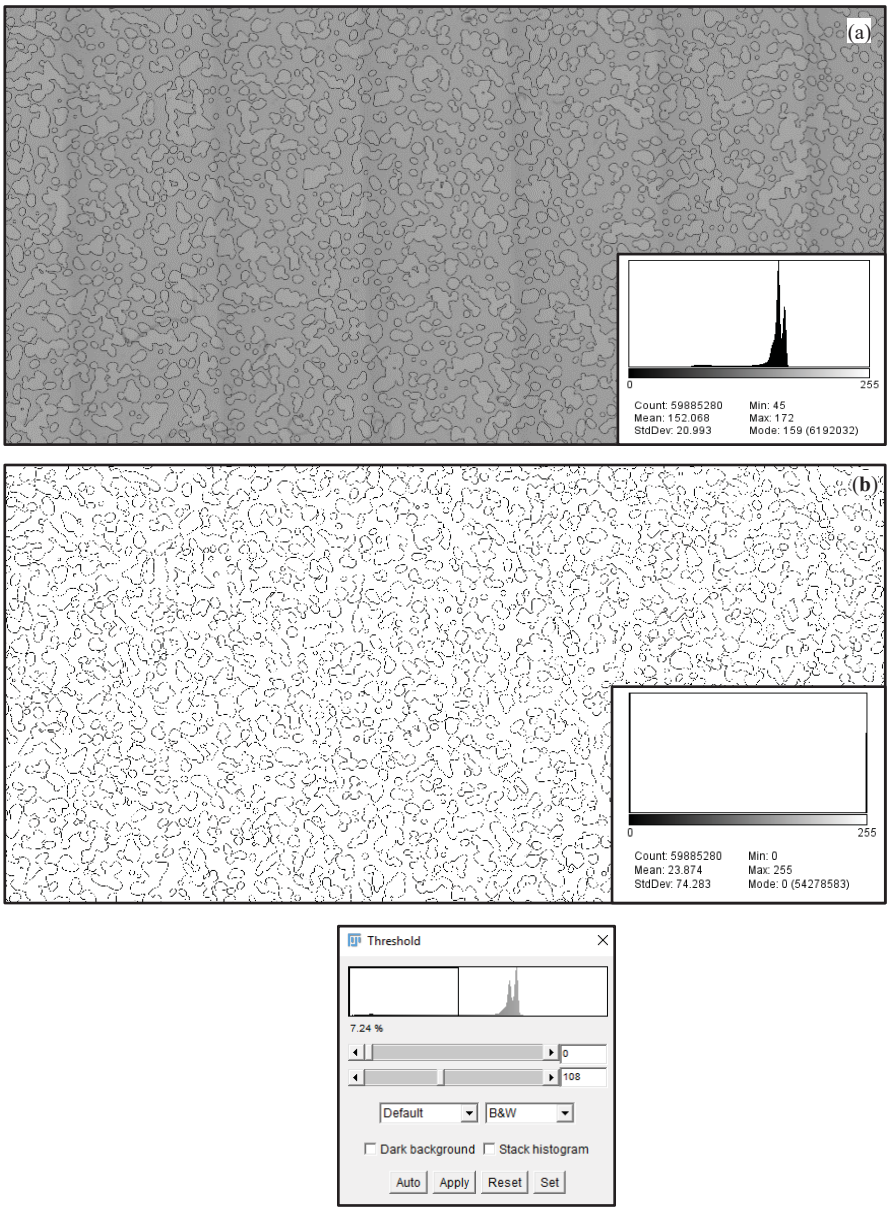

Figure 4-6- Binarizing physical rock micromodel in ImageJ, a) raw image, b) binarized picture

4.3.1 Image workflow to obtain the oil recovery factor

An important information from the performed experiments is the recovery factor. The final RF can be obtained from the last image at the final stage of each experiment. The method is based on (Borji, 2017), where the total pore volume is quantified from the dark area of 100% oil saturated microchip image by image segmentation and area analysis using ImageJ. The measured area corresponds to an oil saturation of 1. The area measured with the same method on a partially oil saturated sample provides the percentage of the pore space saturated with oil. This can be used to measure the remaining oil in the porous medium by equation (4-1):

$$Recovery\ factor = 1 - \frac{area\ of\ remaining\ oil\ at\ final\ stage}{100\ oil\ saturated\ area} \tag{4-1}$$

4.3.2 Image workflow for cluster size analysis

If we have a look to the topology of the remaining oil clusters, we notice that it is organized in oil cluster and droplets (Figure 4-3 and Figure 4-4). The objective of this analysis is to obtain information about these oil clusters and their statistical properties. The main information is Cluster length in the flow direction, cluster volume and oil-water interfaces. The cluster length and volume are based on the pixels.

3D Objective counter Plugin in ImageJ can be used to perform cluster analysis on binarizing images and providing several parameters and maps like:

- The volume of the clusters
- The surface of the clusters
- Center of the clusters mass
- Width in the X direction of the clusters
- Width in the Y direction of the clusters
- Objects map of the clusters
- Centers of masses map of the clusters and … (ImageJ, 2017).

In addition, there are some additional options, which might improve the results. It is possible to define the minimum and maximum of connected pixels defining an object, respectively a cluster. Another option is to exclude objects on the edge of the investigated domain. This is used to remove the clusters, which are not in completely in flood domain or the field of view.

In this thesis, all the images are analyzed with the minimum pixel size of 10 to remove the artifacts from the images, which mainly imposed by artifacts at the grain boundaries. This

plugin detects the disconnected cluster as different objects and for each individual cluster attached different color and number in the objects map. Moreover, the length and area of the cluster, which are applied in the analysis is shown in Figure 4-7. In addition, the objects map image of experiment 1.1 is shown in Figure 4-8, which has 844 clusters.

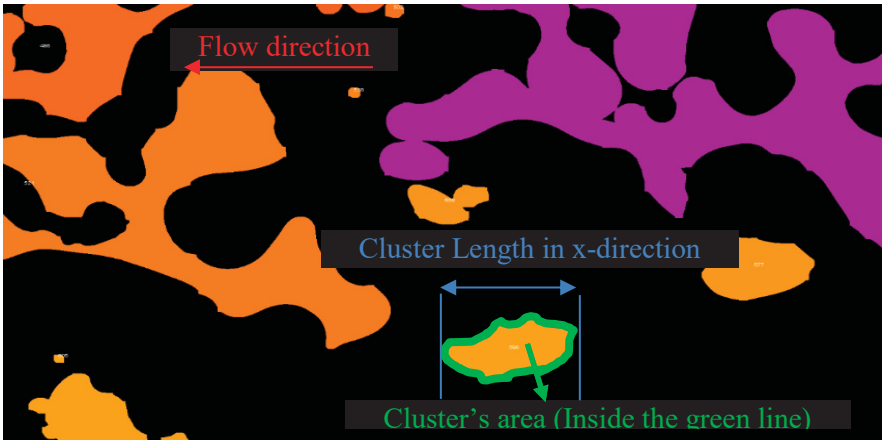

Figure 4-7- Cluster length and area for one individual cluster

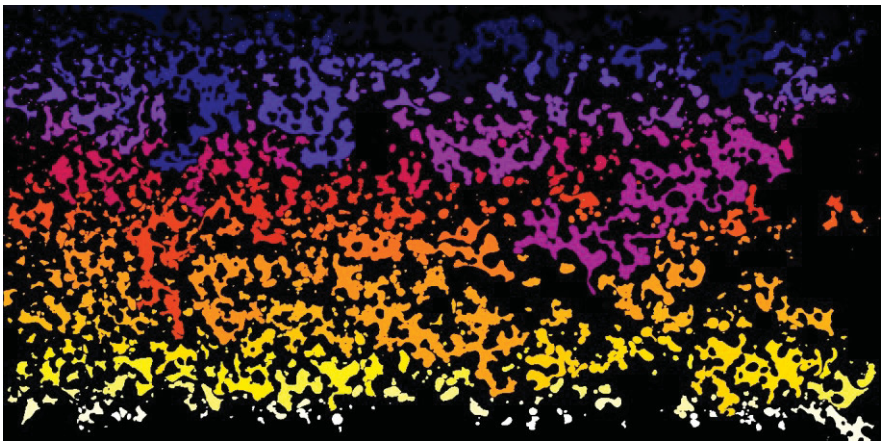

Figure 4-8- Objects map of experiment 1.1

4.4 Discrete frequency distribution analysis

OriginPro data analysis software has been used in this thesis for descriptive statistical analysis. Cluster lengths and volume data are imported into software and by applying the discreet frequency option, the sum of the repeated data is calculated and plotted. Figure 4-9 shows a schematic double logarithmic scale, where the X-axis refers to the cluster size and the Y-axis is the frequency (Ott, 2018). In the upper graph, the frequency is plotted over cluster length, where in the lower one the cluster volume is versus frequency. Moreover, the red line is demonstrating the capillary number equal to one and it is based on the power law and fitted to data by maximum likelihood method (Aaron Clauset, Cosma Rohilla Shalizi, M. E. J. Newman, 2009). For water wet systems (not the present case), the right side of this line refers to mobile

clusters, while the left side refers to immobile clusters. After alkaline flooding, lowering the IFT, the red line can be considered to shift to the left, where the system will be dominated by small clusters, which are more difficult to recover.

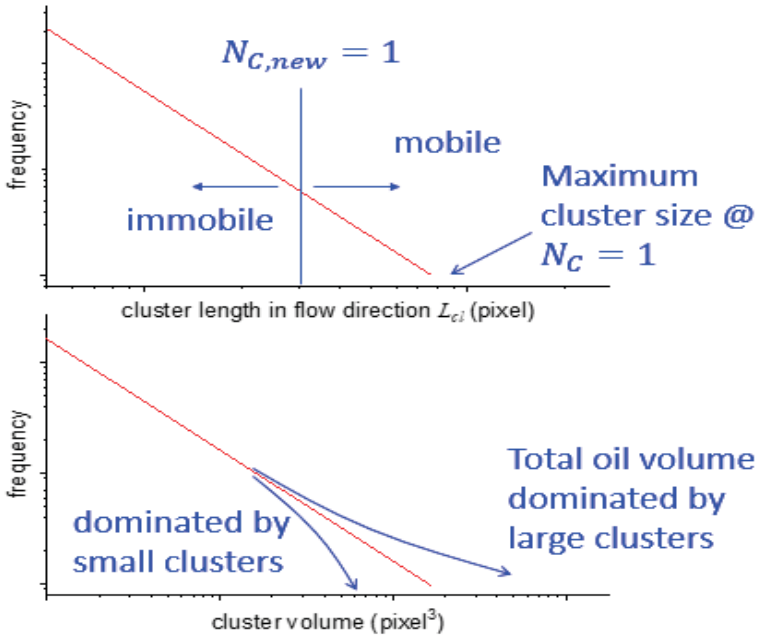

Figure 4-9- Cluster analysis overview (Ott, 2018)

Figure 4-10 shows empirical data from experiment 1, where the wide range of cluster's volume is observed.

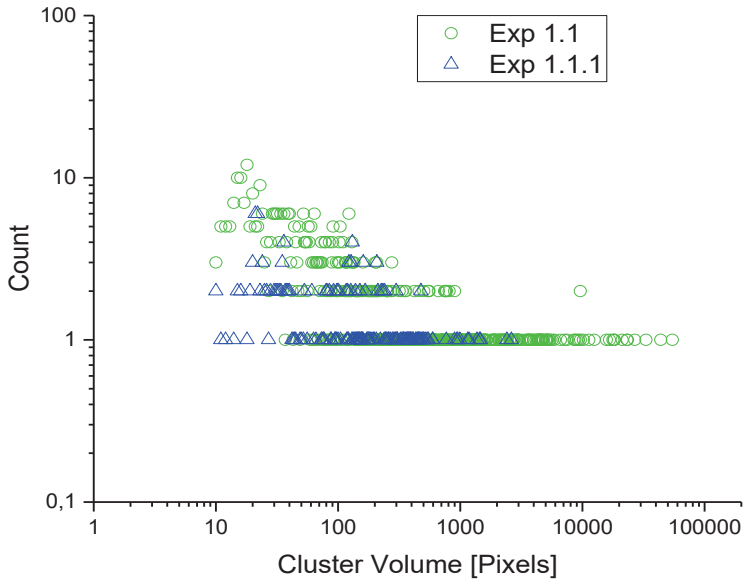

Figure 4-10- Frequency and cluster volume sizes distribution of experiment 1

The scatter is essentially removed and data are normalized by calculating the cumulative cluster size distribution by numerical integration of the discrete data set by Equation (4-2). The cumulative size distribution following a power law behavior. Therefore, by using maximum likelihood method a power law function is fitted to data. This calculation was carried out by MATLAB code (Aaron Clauset, Cosma Rohilla Shalizi, M. E. J. Newman, 2009). P(x) is the fraction of cluster whose volume is at least x, which is a cumulative probability. Figure 4-11 is an example of the normalizing distribution. From this graph, it could be stated that 70% of clusters in the waterflooding have at least 100 pixels of volume oil inside.

$$P(x) = \int_x^{\infty} C_y^{-\alpha}\, dy = \left(\frac{x}{x_{min}}\right)^{-\alpha+1} \tag{4-2}$$

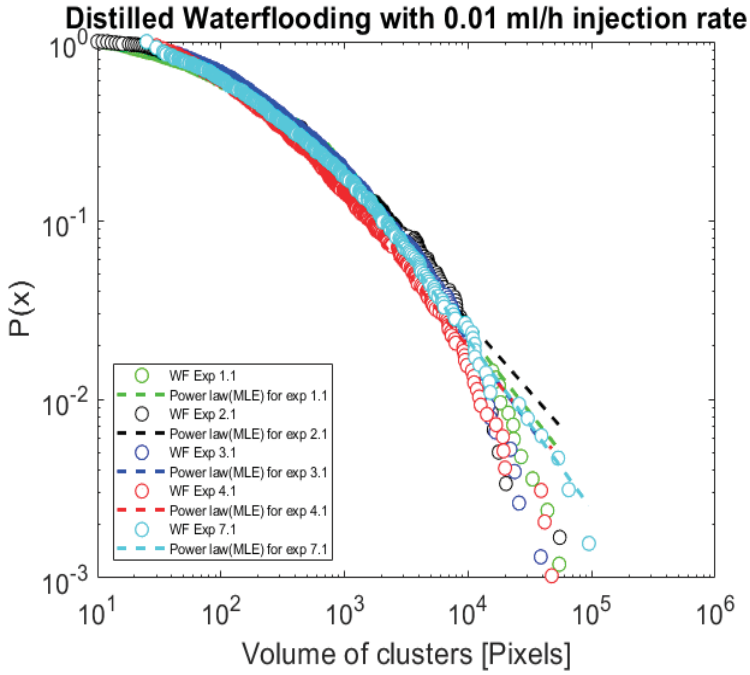

Figure 4-11- Normal distribution of distilled WF with 0.01 ml/h

4.5 Lorenz curve analysis

Max Otto Lorenz is an economist, who developed the Lorenz curve. The main idea behind this curve is to illustrate the wealth distribution in society, while in oil industry this plot is mostly used to quantify heterogeneity of the rock formations. In this work, the graph is used for the first time comparing the distribution of the clusters and their volumes. The MATLAB code is developed to achieve the desired plots. The X-axis of the graph is the fraction of clusters based on their sizes (P(x)) and the Y-axis is the volume of the oil inside the clusters (W(x)), which is shown in Figure 4-12. The blue line is Lorenz plot for experiment 1.1, as the curve tends in

direction of the red line, the potential of oil recovery increases as a large amount of oil volume is sitting in a small fraction of cluster. In contrary, the green line indicates a homogenous and equal distribution of oil volume over clusters sizes.

The volume weighted cumulative cluster size distribution, W(x), is calculated by equation (4-3):

$$W(x) = \frac{\int_x^{\infty} y\, p(y)\ \ dy}{\int_{x_{min}}^{\infty} y\, p(y)\, dy} = \left(\frac{x}{x_{min}}\right)^{-\alpha+2} \tag{4-3}$$

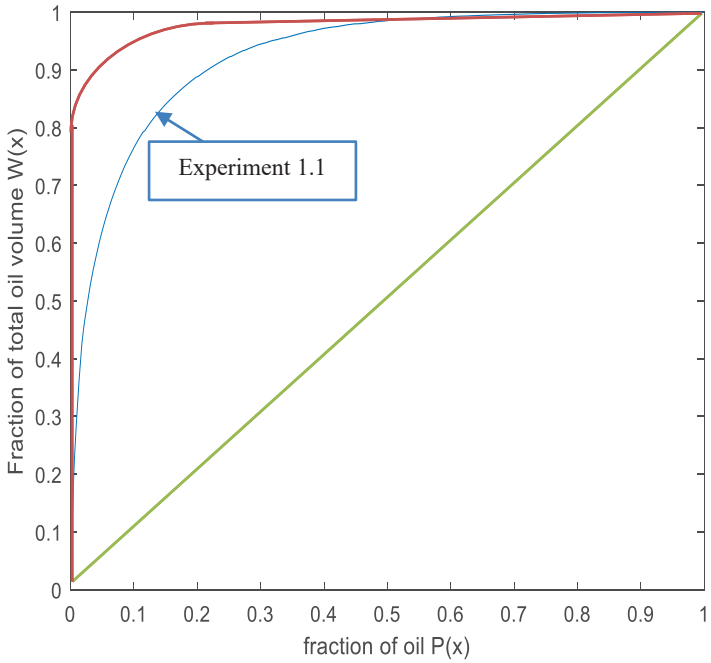

Figure 4-12- Lorenz plot of experiment 1.1

Chapter 5

Results and Discussion

In this chapter, the results of all experiments and their analyses will be discussed. The experiments are divided based on the used microchip pattern and the applied injection rate. It should be mentioned that the analyses are carried out on the last stage of each experiment, which is obtained approximately 22 hours after water flooding and 24 hours after alkaline flooding.

5.1 Ultimate Recovery factor results

Recovery factors are calculated based on the on the imaging and image analysis workflow as discussed above by equation (4-1).

Total recovery factor for physical rock pattern

Several alkaline floods were investigated by using the physical rock pattern. Water flooding has been performed by injecting distilled or synthetic water at two flow rates, 0.01 and 0.001 ml/h, which resulted in different recovery factors. Subsequently, alkalic solutions were injected for tertiary recovery. The obtained ultimate recoveries are listed in Table 5-1 and Table 5-2.

Table 5-1- Recovery factor for physical rock pattern with 0.01 ml/h

Experiments	Water flooding	Alkaline flooding	Tertiary RF [%]	Ultimate RF [%]
Experiment 1.1	Distilled water			36
Experiment 1.1.1		3000 ppm Na_2CO_3 with distilled water	93	97
Experiment 2.1	Distilled water			55
Experiment 2.1.1		3000 ppm Na_2CO_3 with distilled water	88	95
Experiment 3.1	Distilled water			43
Experiment 3.1.1		7500 ppm Na_2CO_3 with distilled water	80	89
Experiment 4.1	Distilled water			36
Experiment 4.1.1		7500 ppm Na_2CO_3 with distilled water	79	87
Experiment 5.1	Synthetic water			75
Experiment 5.1.1		3000 ppm Na_2CO_3 with synthetic water	39	85
Experiment 6.1	Synthetic water			80
Experiment 6.1.1		7500 ppm Na_2CO_3 with synthetic water	30	95
Experiment 7.1	Distilled water			44
Experiment 7.1.1		720 ppm NaOH with distilled water	91	95
Experiment 8.1	Distilled water			40

Table 5-2- Recovery factor for physical rock pattern with 0.001 ml/h

Experiments	Water flooding	Alkaline flooding	Tertiary RF [%]	Ultimate RF [%]
Experiment 9.1	Distilled water			41
Experiment 9.1.1		720 ppm NaOH with distilled water	51	70
Experiment 12.1	Distilled water			45
Experiment 12.1.1		6000 ppm Na2CO3 with distilled water	74	86

As can be seen in all runs, the addition of alkaline has enhanced the recovery of oil as expected.

Recovery factor in the uniform pattern

The uniform pattern represents a more capillary dominated system at the same flow rate compared to the physical rock pattern. Three series of experiments have been performed at a flow rate of 0.001 ml/h. Experimental details and the resulting recovery factors are shown in Table 5-3.

Table 5-3- Recovery factor for the uniform pattern with 0.001 ml/hr.

Experiments	Water flooding	Alkaline flooding	Tertiary RF [%]	Ultimate RF [%]
Experiment 10.1	Distilled water			50
Experiment 10.1.1		720 ppm NaOH with distilled water	1	52
Experiment 11.1	Distilled water			46
Experiment 11.1.1		950 ppm Na_2CO_3 with distilled water	2	47
Experiment 13.1	Distilled water			38
Experiment 13.1.1		6000 ppm Na2CO3 with distilled water	56	65

The results are plotted and discussed in the following. Upfront we can say that alkaline flooding in uniform pattern shows generally smaller recovery factors compare to the results on the physical rock pattern. The underlying reasons for low recovery factor might be that capillary forces in the uniform pattern are greater, facilitating capillary fingering and breakthrough.

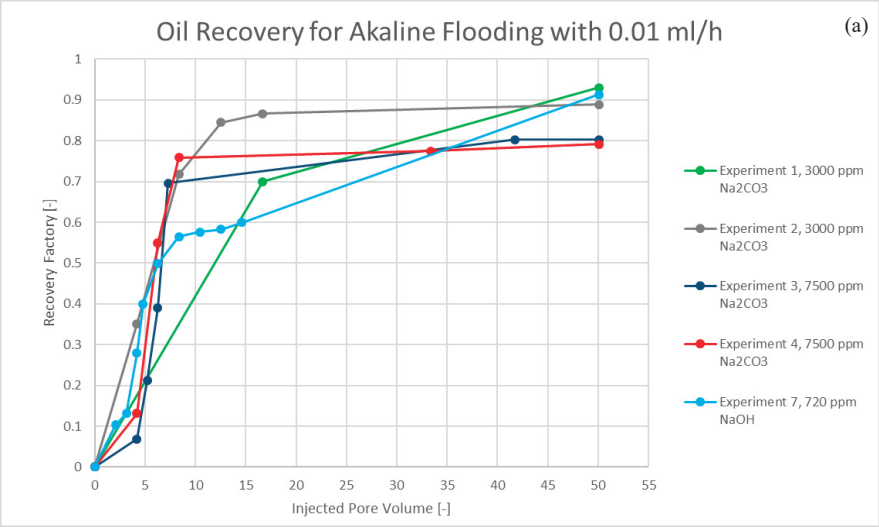

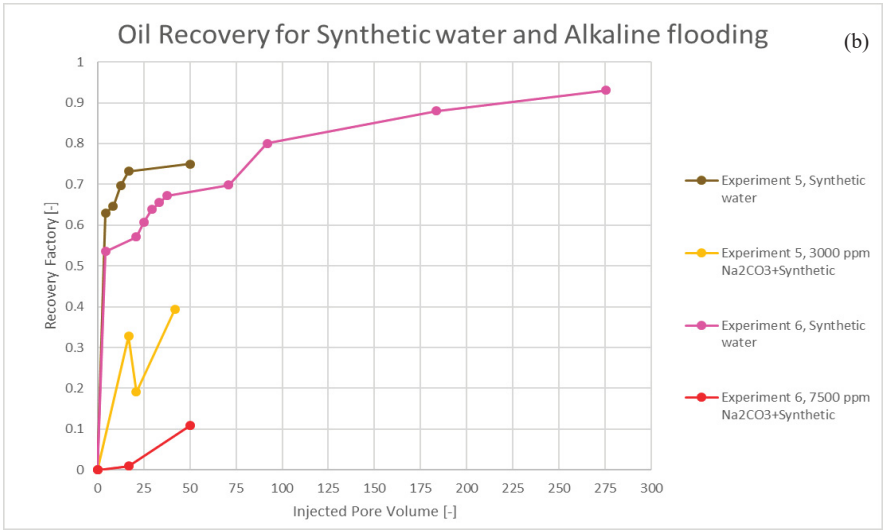
Oil Recovery for Synthetic water and Alkaline flooding
(b)
Recovery Factory [-]
Injected Pore Volume [-]
Experiment 5, Synthetic water
Experiment 5, 3000 ppm Na2CO3+Synthetic
Experiment 6, Synthetic water
Experiment 6, 7500 ppm Na2CO3+Synthetic

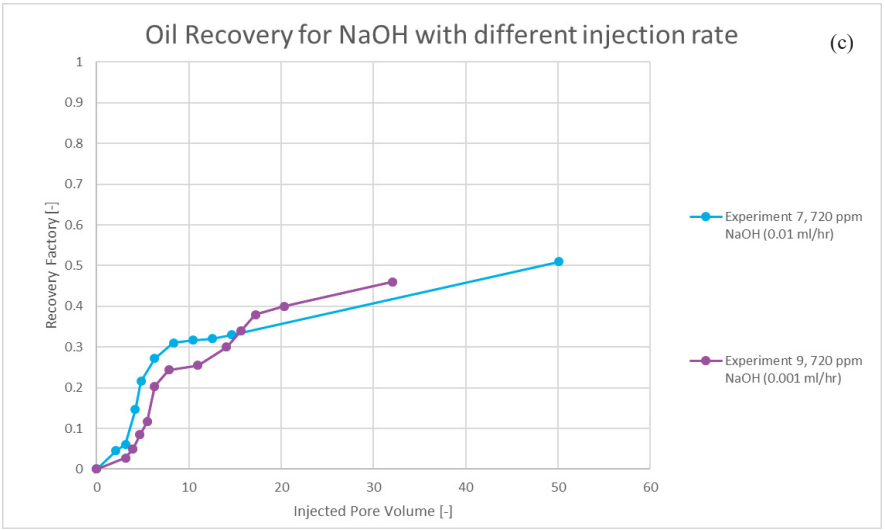
Oil Recovery for NaOH with different injection rate
(c)
Recovery Factory [-]
Injected Pore Volume [-]
Experiment 7, 720 ppm NaOH (0.01 ml/hr)
Experiment 9, 720 ppm NaOH (0.001 ml/hr)

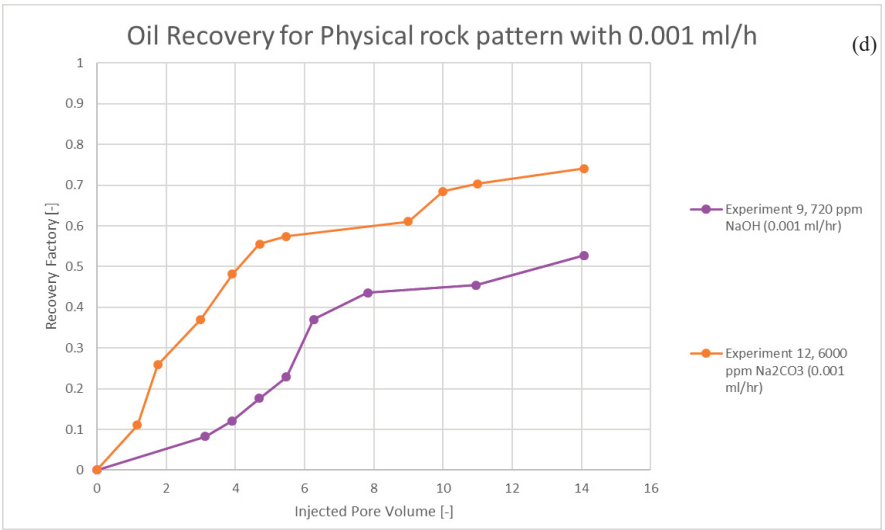
Oil Recovery for Physical rock pattern with 0.001 ml/h
(d)
Recovery Factory [-]
Injected Pore Volume [-]
Experiment 9, 720 ppm NaOH (0.001 ml/hr)
Experiment 12, 6000 ppm Na2CO3 (0.001 ml/hr)

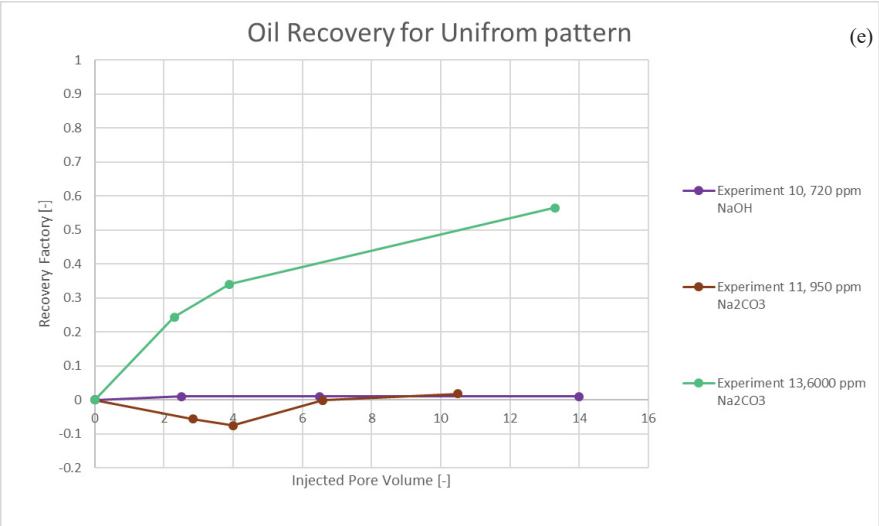

Figure 5-1- Remaining oil recovery in tertiary flooding for, a) Solution with distilled water, b) Solution with synthetic water, c) 720 ppm NaOH with different injection rate, d) in Physical rock with 0.001 ml/h injection rate, e) in Uniform with 0.001 ml/h

Figure 5-1-a illustrates that oil production significantly increases between 5-10 pore volumes injection in all the floods (in experiment 1 (3000 ppm Na_2CO_3), the point density does not allow for this statement). Moreover, experiments 3 and 4, performed with the same alkaline solution of 7500 ppm Na_2CO_3 under the same conditions was nicely repeatable. Experiments 1 and 2 (3000 ppm Na_2CO_3), are difficult to compare due to the different point density of the two data sets. Additionally, experiment 7 (720 ppm NaOH) illustrates a smoother gradient for recovery factor compare to other floods, which yields to a smaller amount of oil produced at early times i.e. at lower pore volume injected.

In Figure 5-1-b, oil production is in a direct relationship with injected pore volume for synthetic water injection. During the displacement, oil clusters elongated and become a connected phase, which declines the rate of oil recovery. Therefore, the oil is produced even after 200 pore volume injection. Additionally, oil is displaced from the inlet of micromodel into the system and change the saturation and distribution of oil during the flooding. This is also demonstrated in experiment 5 (3000 ppm Na_2CO_3 solution with synthetic water), where the recovery declines as oil enter to the micromodel. Moreover, both alkaline solution with synthetic water resulted in a comparably low additional recovery due to the good oil displacement already in the secondary water flood using synthetic water.

Figure 5-1-c displays the tertiary oil recovery for 720 ppm NaOH with 0.01 and 0.001 ml/h injection rates. The recovery factor in both floodings is significant. However, experiment 9 (0.001 ml/h) yields in a lower value; the small oil clusters remain in the micromodel indicating a lower displacement efficiency compare to experiment 7 (0.01 ml/h).

Experiments 12 (6000 ppm Na_2CO_3) yielded in a higher recovery factor after the same flooding time, i.e. the same injected pore volume compare to experiments 9 (720 ppm NaOH) (Figure 5-1-d). Additionally, the peak of the oil production rate for both flooding occurs between 2-6 pore volume injections.

Surprisingly, experiments in the uniform pattern show an entirely different behavior compared to experiments on the physical rock pattern. Also, the experiments amongst each other were quite different to compare and show different trends with respect to recovery as can be seen in Figure 5-1-e. As already mentioned, capillary fingering seems to be the main reasons for this performance, which will be discussed further below. In addition, during the alkaline flooding, the oil is displaced from the inlet channel and distributed again into micromodels, which could explain the apparently negative recovery in experiment 11 (9500 ppm Na_2CO_3).

5.2 Advance Statistical analyses

As it has been shown in the previous, the ultimate recovery shows quite some scatter and variation for repeat experiments and is therefore just of limited use for the characterization of water flooding and EOR from small-scale microfluidics. The reason is likely in the natural variation of the boundary conditions (inlet, outlet oil/water distribution) and the volume of the flooding domain, which may not be a representative elementary volume (for two-phase flow). Since this number is calculated from the images, an error from image processing might have an impact on the results as well. Therefore, statistical data analyses are used in the following to compare results from the different experiment.

In the following, I discuss the system properties and analysis methods employed in this thesis: the recovery factor, the frequency of cluster volume and length, the cumulative distributions with estimated power law exponent and Lorenz plots. The experiments are divided and discussed in different categories:

- Waterflooding with 0.01 ml/h rate in physical rock pattern
- Alkaline flooding with 0.01 ml/h rate in physical rock pattern
- Different injection rate in physical rock pattern
- Alkaline flooding with 0.001 ml/h rate in physical rock pattern
- Flooding in the uniform pattern
- Comparison between two patterns

5.2.1 Waterflooding with 0.01 ml/h rate in physical rock pattern

In this section, I re-discuss the results on the waterflooding for distilled and synthetic water with 0.01 ml/h injection rate.

Distilled and synthetic water comparison

The range of recovery factors for flooding with distillate water were observed between 36 and 55% with the average being 44%. This is in strong contrast to flooding with synthetic water, where a much higher average value of 78% was observed. It should be mentioned that for distilled waterflooding the production rate dropped relatively fast with no measurable production after 22h of injection (Figure 5-2-a). In contrast, synthetic water flooding led to measurable oil production even after 22 hours of flooding time. This fact is illustrated by comparing Figure 5-2-b and Figure 5-2-c and also visible in the production curves discussed above. This might be due to the wettability alteration effects, which are different for distilled and synthetic water flooding. In the synthetic case, a wetting change to a more water wet system led to the formation of larger clusters with an apparently lower mobility, which taking longer time being recovered.

The IFT of distilled water and crude oil has been determined to 0.35 mN/m, while the IFT of Synthetic water with crude oil to around 0.032 mN/m (Arnold, 2018). The observed droplet shape can be compared to the droplet formation as observed in spinning drop experiments by (Arnold, 2018). It should be mentioned that the same water compositions and the same oil type were used in both works. Even though the type of experiments cannot really be compared. The observed droplet shapes show similarities that I want to point out. This is illustrated in Figure 5-3 and Figure 5-4 where droplets during water flooding are elongated in the horizontal direction as the generated droplet in Arnold's work. The droplets observed in both types of experiments where whether equidistantly spaced in case of distilled water, as there would be a repulsive force between the droplets. In contrast, in the synthetic case, droplets seem to join together. The dissimilarity between synthetic and distilled water is shown in Figure 5-5, where the final stage for most of the floods is not comparable.

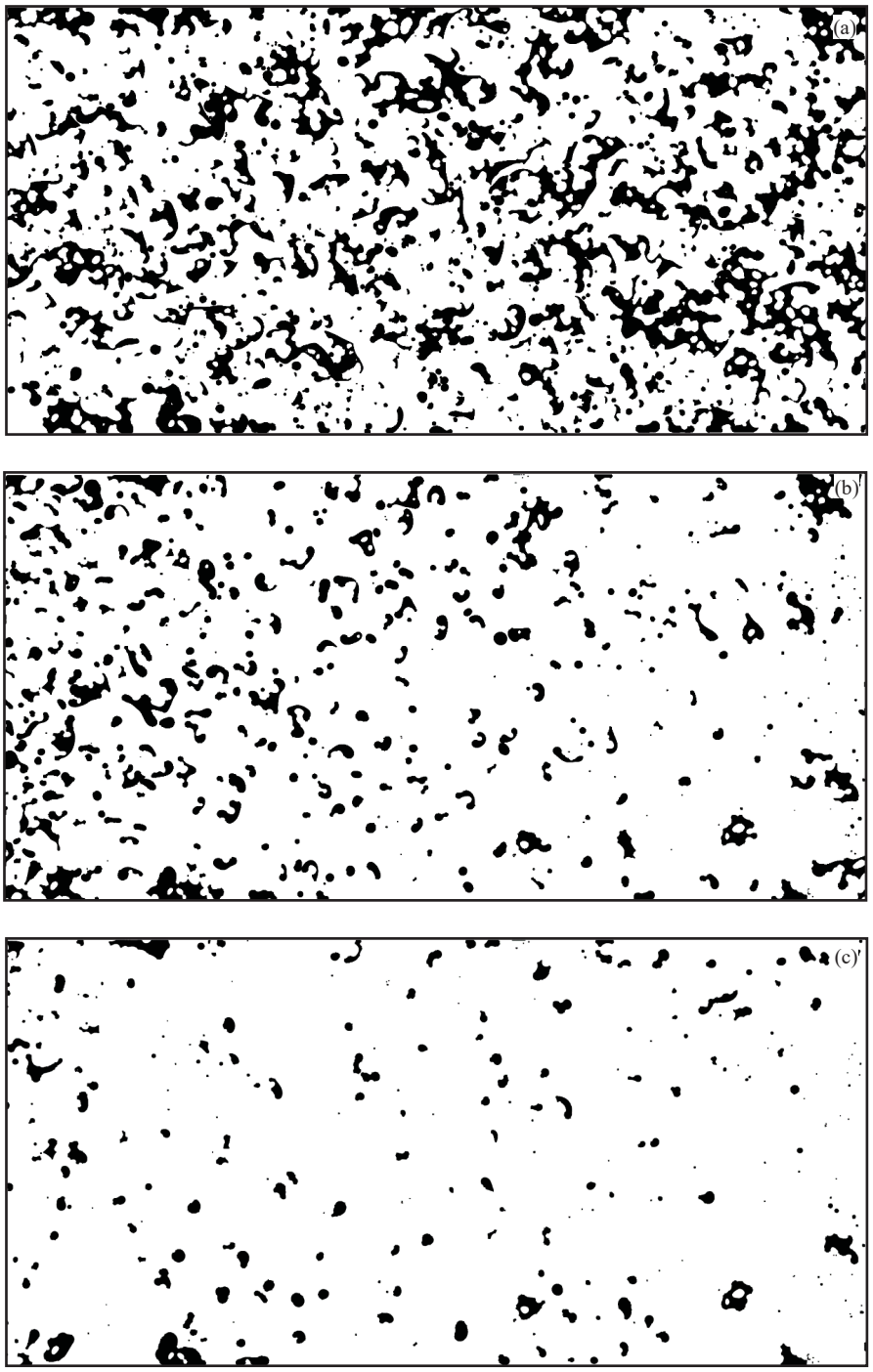

Figure 5-2- Binary Image of a) distilled water flooding (experiment 2.1), b) synthetic water flooding (experiment 6.1) after 22 hours, c) synthetic water flooding (experiment 6.1) after 62 hours

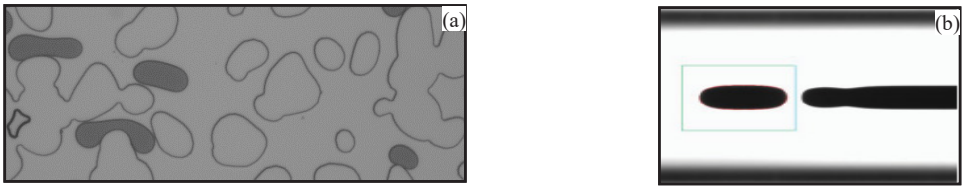

Figure 5-3-a) Tile picture crude oi1 and distilled water, b) IFT measurement of distilled water and crude oil with the spinning drop (Arnold, 2018)

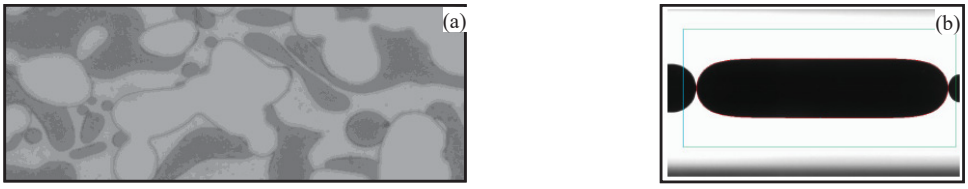

Figure 5-4-a) Tile picture crude oi1 and synthetic water, b) IFT measurement of synthetic water and crude oil with the spinning drop (Arnold, 2018)

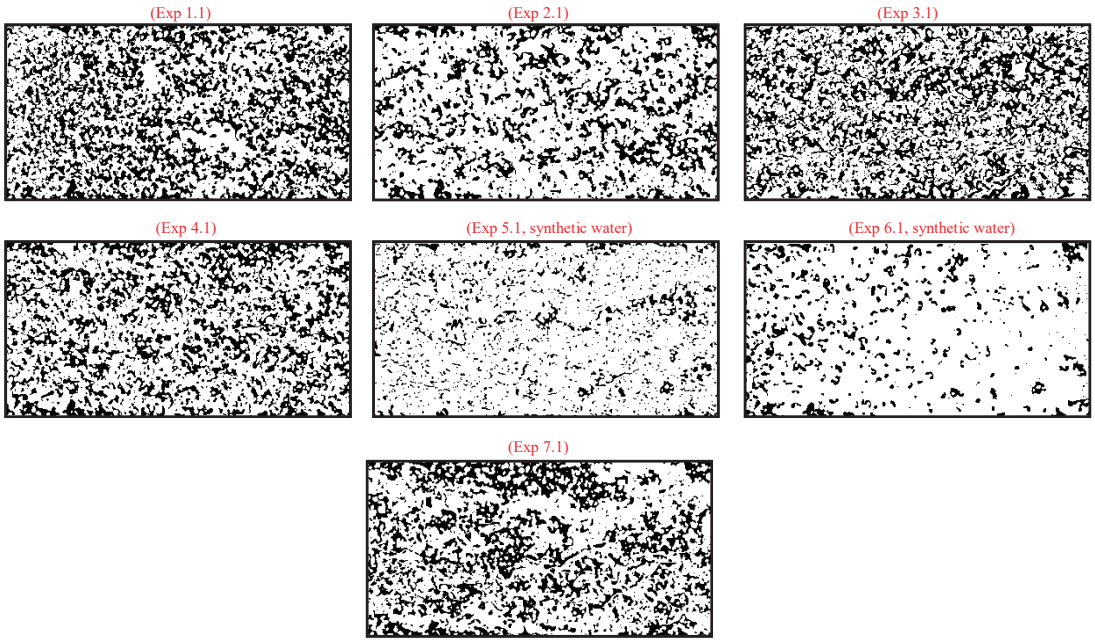

Figure 5-5- The final stage of all the water flooding with 0.01 ml/h

The distilled water flooding mainly generates smaller cluster compared to synthetic water flooding, while the minimum cluster volume in the synthetic case with the smallest clusters being 100 pixels in size. This behavior is more noticeable in Figure 5-6-b. Furthermore, based on the Lorenz plot, the synthetic water case shows a more equal distribution of the oil cluster sizes than distilled water, which is illustrated in Figure 5-6-c.

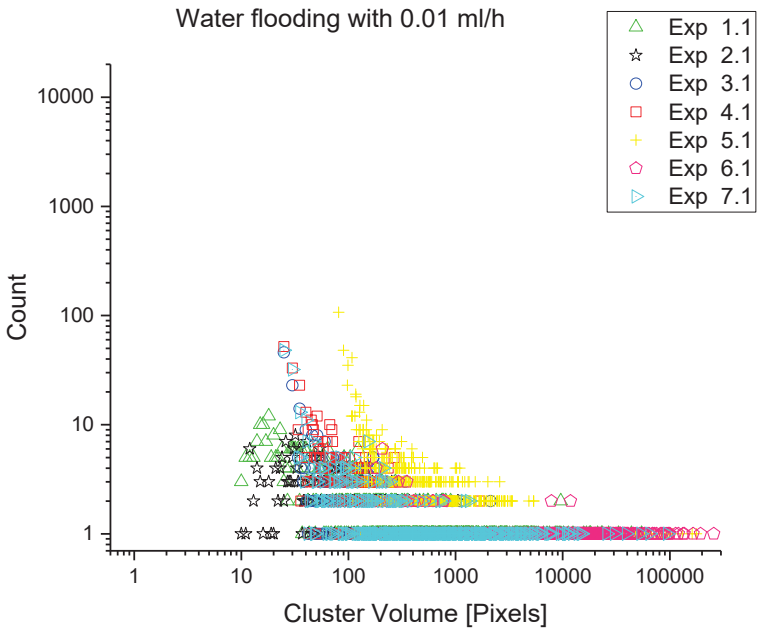
Water flooding with 0.01 ml/h
Exp 1.1
Exp 2.1
Exp 3.1
Exp 4.1
Exp 5.1
Exp 6.1
Exp 7.1
Count
Cluster Volume [Pixels]

(a)

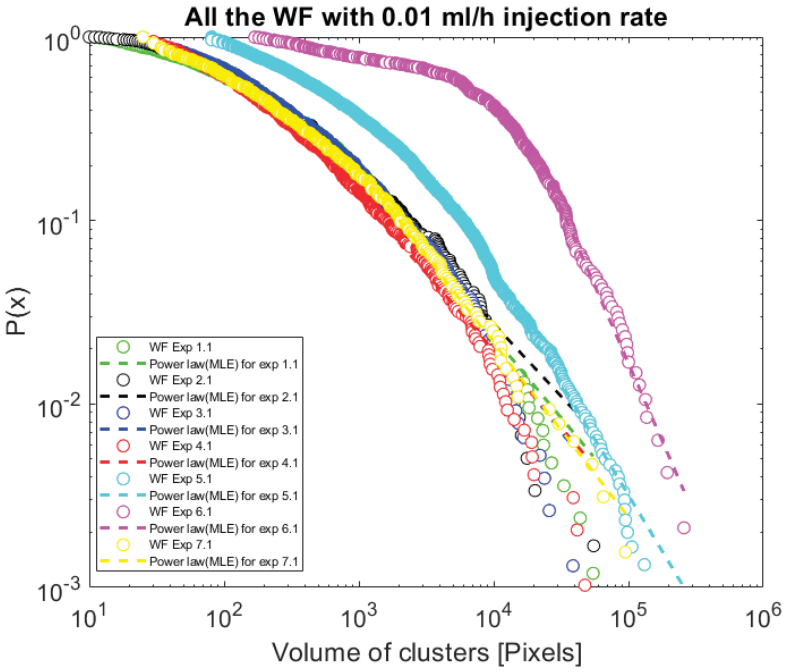
All the WF with 0.01 ml/h injection rate
P(x)
Volume of clusters [Pixels]
WF Exp 1.1
Power law(MLE) for exp 1.1
WF Exp 2.1
Power law(MLE) for exp 2.1
WF Exp 3.1
Power law(MLE) for exp 3.1
WF Exp 4.1
Power law(MLE) for exp 4.1
WF Exp 5.1
Power law(MLE) for exp 5.1
WF Exp 6.1
Power law(MLE) for exp 6.1
WF Exp 7.1
Power law(MLE) for exp 7.1

(b)

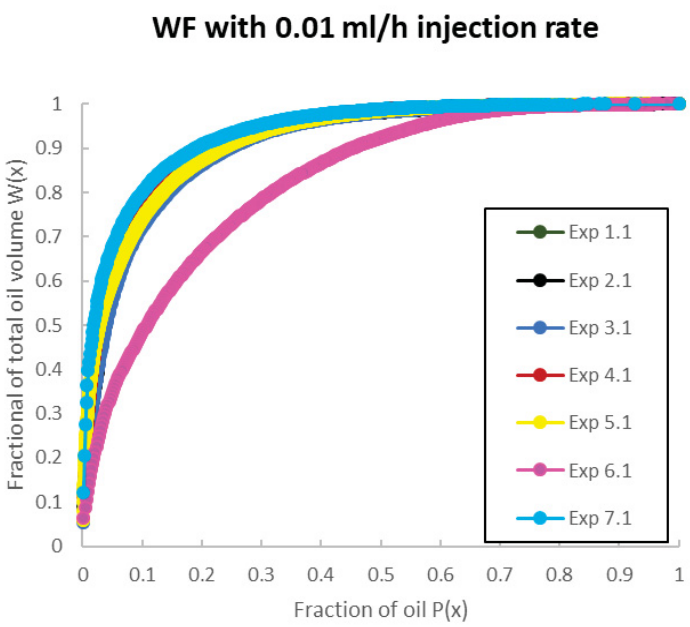

Figure 5-6- Statistical analyses for waterflooding with 0.01 ml/h, a) cluster size distribution, b) Normalize distribution c) b) Lorenz plot

As it was mentioned earlier, during distilled water flooding, some of the oil remained in the inlet channels without entering the porous domain. The remaining oil volume and the locations of the oil in the injection channels varied for different water compositions and were observed to be different for synthetic and distilled water. The synthetic water acted in a similar way that alkali solutions. The oil in the injection channels was displaced in the first stage of the experiments with no further oil entering the porous domain during water flooding. In contrast, the oil was invading the micromodel randomly 2-3 times during a synthetic water flood. This performance is illustrated in time steps in Figure 5-7.

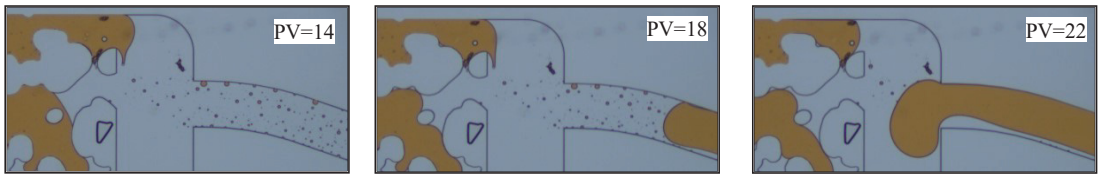

Figure 5-7- Oil entering micromodel during waterflooding, time steps is from left to right

Distilled water comparison

The main variation in recovery factors linked to distilled water flooding, which was about 20%. However, the cluster size distribution shows a scatter which is comparable for all experiments, but with certain characteristic differences as shown in Figure 5-8-a. An example is experiment 1.1 and 2.1, in which more smaller clusters were generated during flooding than in the other experiments. This can more clearly be observed as starting point of the cumulative distribution

in Figure 5-8-b. In addition, the power law exponents fitted to the tale are similar for all the experiments. From the Lorenz plot, it can be stated that the oil phase volume is dominated by a small fraction of rather large clusters – a rather unequal distribution, which may indicate a good EOR potential (Figure 5-8-c).

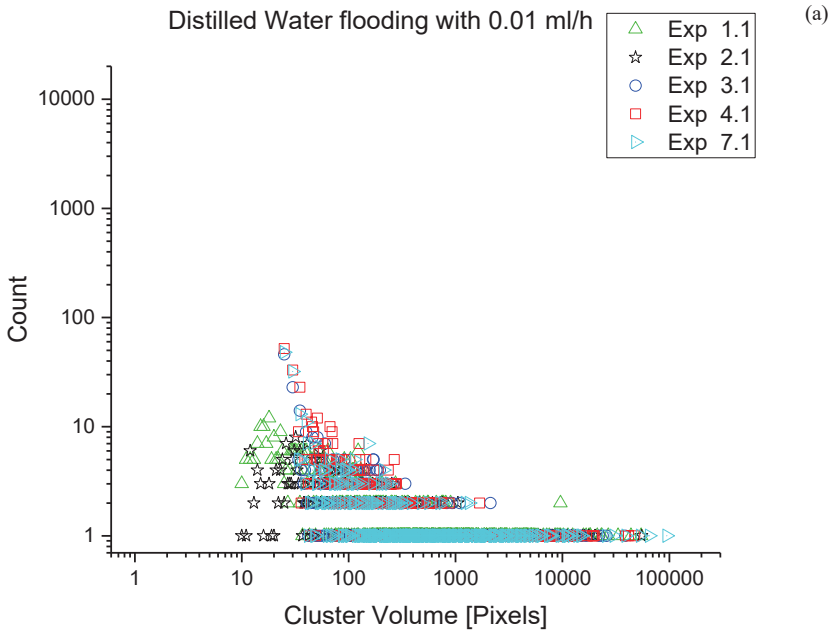

(a)

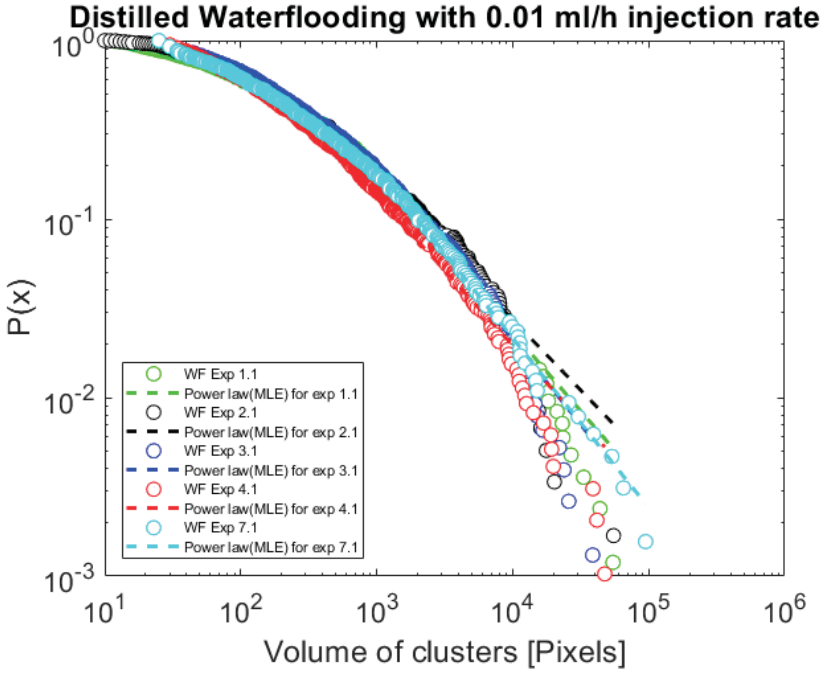

(b)

(c)

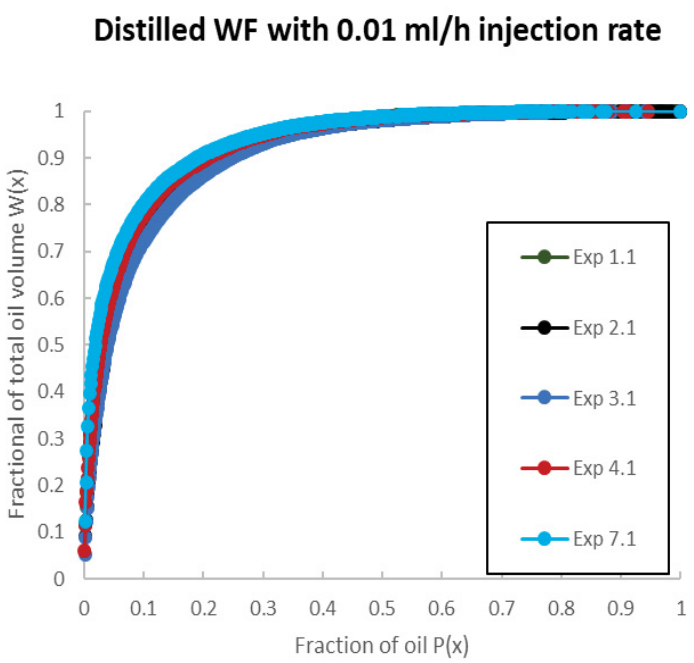

Figure 5-8- Statistical analyses for Distilled waterflooding with 0.01 ml/h, a) cluster size distribution, b) Normalize distribution, c) Lorenz plot

A Lorenz plot analysis has also been applied to Experiment 1.1.1 (waterflood) of an experiment done by (Borji, 2017) to compare both twin experiments statistically. Figure 5-9 and Figure 5-10 show the Lorenz plot and final stage of waterflooding, respectively.

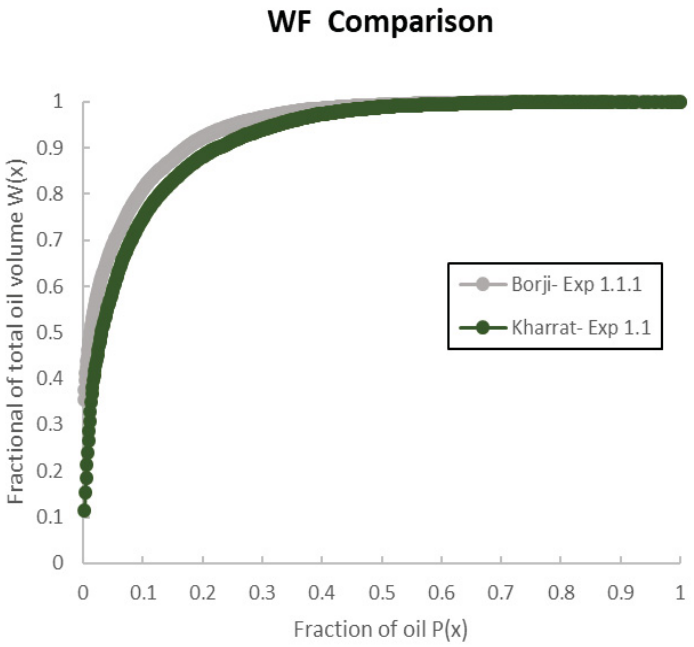

Figure 5-9- Comparison of water flooding with Lorenz plot

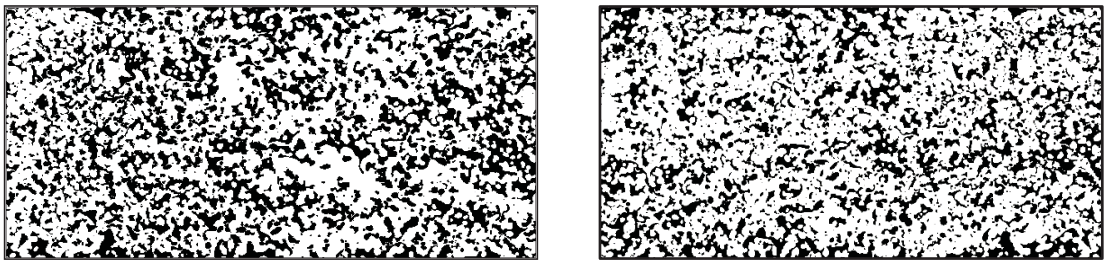

Figure 5-10- The last stage of water flooding for a) Exp 1.1 (this thesis), b) Exp 1.1.1 (Borji, 2017)

5.2.2 Alkaline flooding with 0.01 ml/h rate in physical rock pattern

Results of alkaline flooding in Experiments 1 to 7 are discussed and compared in this part.

Alkaline flooding with 3000 ppm Na_2CO_3 (Experiment 1 and 2)

The location of the remaining oil phase in the final-stage images was different for each experiment, while the observed recovery factors were not too different (exp 1.1.1 =93%, exp 2.1.1= 88%). This similarity is also observed in the statistical cluster analyses. Figure 5-11-a displays the cluster volume distribution for both experiments which show a similar behavior and scatter. This could also be seen in Figure 5-11-d, where the curves for both alkaline floods follow similar trends and the oil volume is tended to be more homogenously distributed in cluster sizes. It was observed that during alkaline flooding, large oil clusters brake into smaller droplets, being displaced by the injection water more easily.

Additionally, the right side of Figure 5-11-b demonstrates that the cluster volume tends to a narrower distribution on expense of larger clusters for the alkaline case compared to distilled water flooding. This behavior is also observed in Figure 5-11-c, where the exponent of the power law for alkaline flooding significantly deviates from the one of water flooding. Figure 5-12 shows the final segmented images of 3000 ppm sodium carbonate alkaline floods, where visually a significant number of small oil clusters is noticeable.

(a)

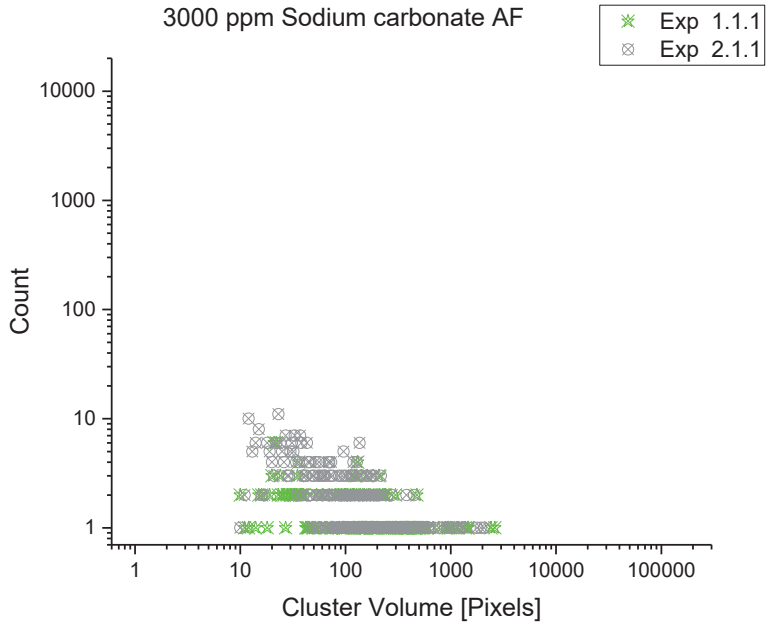
3000 ppm Sodium carbonate AF
Exp 1.1.1
Exp 2.1.1
Count
10000
1000
100
10
1
1
10
100
1000
10000
100000
Cluster Volume [Pixels]

(b)

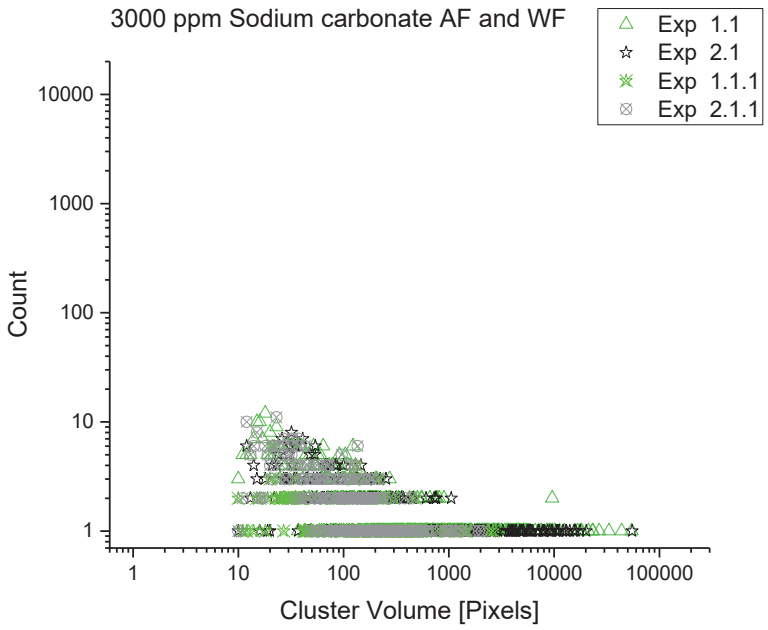
3000 ppm Sodium carbonate AF and WF
Exp 1.1
Exp 2.1
Exp 1.1.1
Exp 2.1.1
Count
10000
1000
100
10
1
1
10
100
1000
10000
100000
Cluster Volume [Pixels]

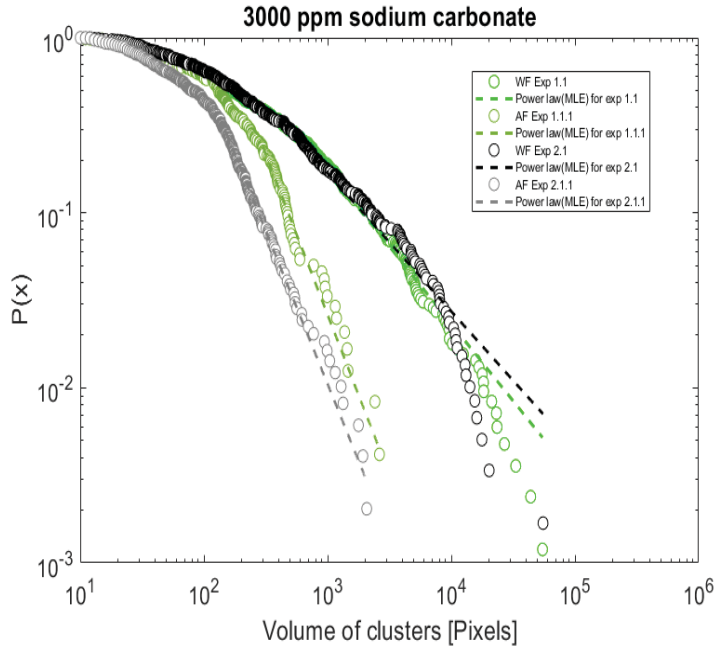

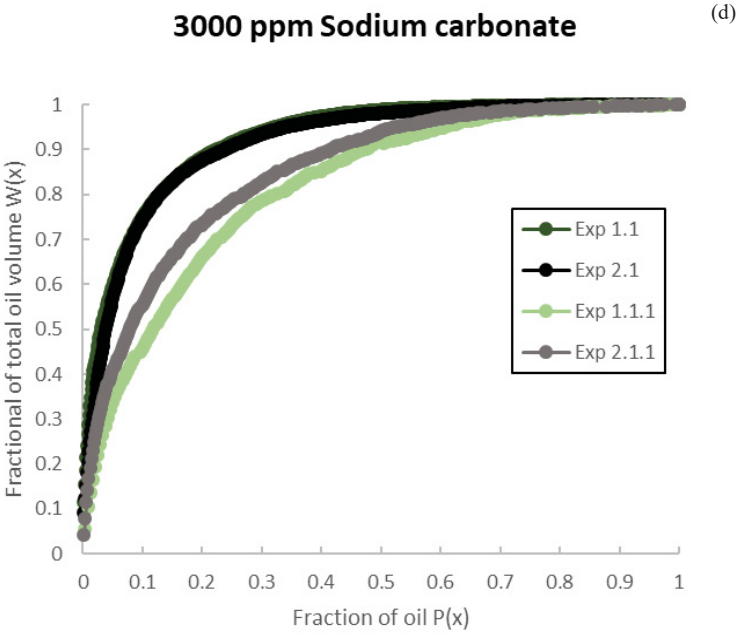

Figure 5-11- Statistical analyses for 3000 ppm Na_2CO_3 a) cluster size distribution for AF, b) cluster size distribution for WF and AF, c) Normalize distribution, d) Lorenz plot

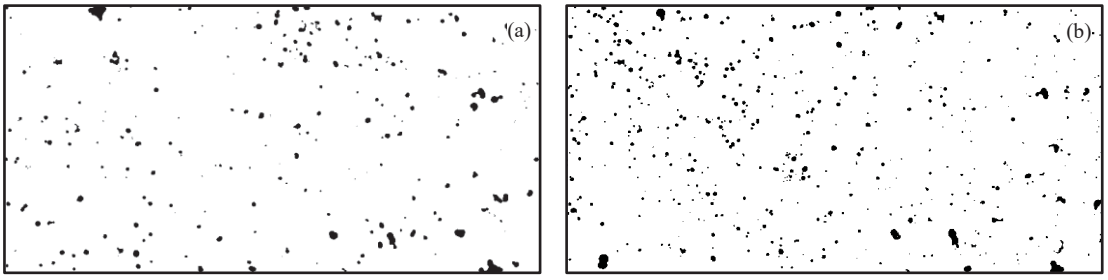

Figure 5-12- Last stage of 3000 ppm flooding Na_2CO_3, a) Exp 1.1.1, b) Exp 2.1.1

Alkaline flooding with 7500 ppm Na_2CO_3 (Experiments 3 and 4)

Both of the following 7500 ppm Na_2CO_3 alkaline flooding experiments were repeatable in the sense of recovery which was 80% for both, and also from the cluster statistical point of view, even if the left image shows a large remaining cluster not observed in the right image (Figure 5-13). This is reflected in the images. Figure 5-14 discussing the statistical cluster properties. With respect to the time dependent displacement, larger clusters break into smaller clusters, which are mobile and finally recovered. However, even with similar cluster size distribution (Figure 5-14-a), higher alkaline concentration generates larger clusters compared to 3000 ppm Na_2CO_3 (comparing Figure 5-13 and Figure 5-13). The larger clusters and the resulting lower recovery are due to microemulsion formation, which is pinning the clusters to the solid boundaries. Overall, despite the discussed differences, the observed behavior is very similar to that observed for the lower concentration of 3000 ppm Na_2CO_3.

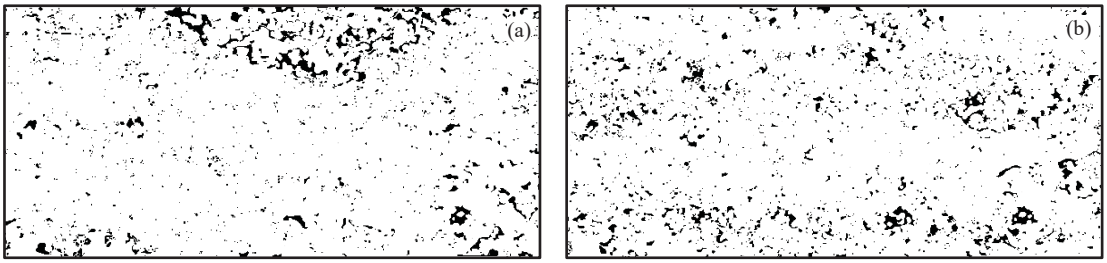

Figure 5-13- Last stage of 7500 ppm Na2CO3 flooding a) Exp 3.1.1, b) Exp 4.1.1

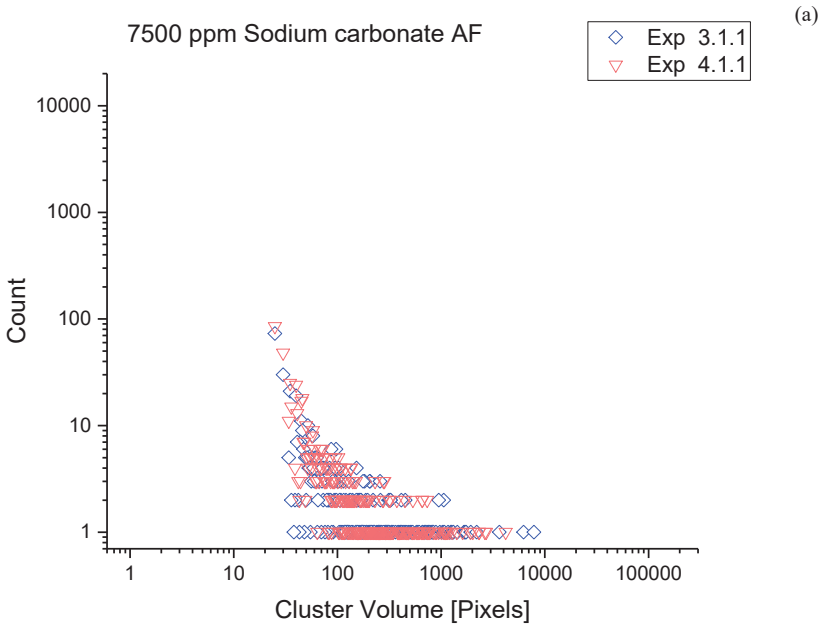

(b)

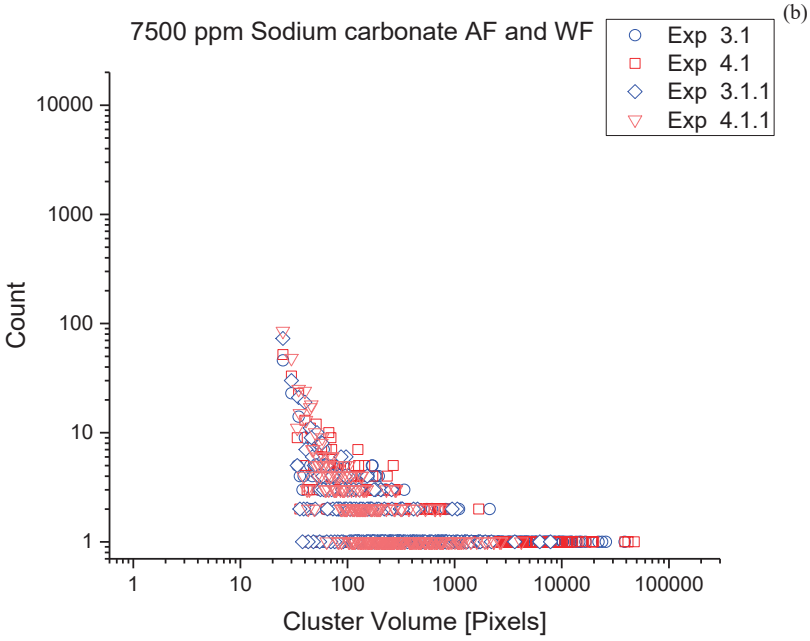
7500 ppm Sodium carbonate AF and WF
Exp 3.1
Exp 4.1
Exp 3.1.1
Exp 4.1.1
Count
10000
1000
100
10
1
1
10
100
1000
10000
100000
Cluster Volume [Pixels]

(c)

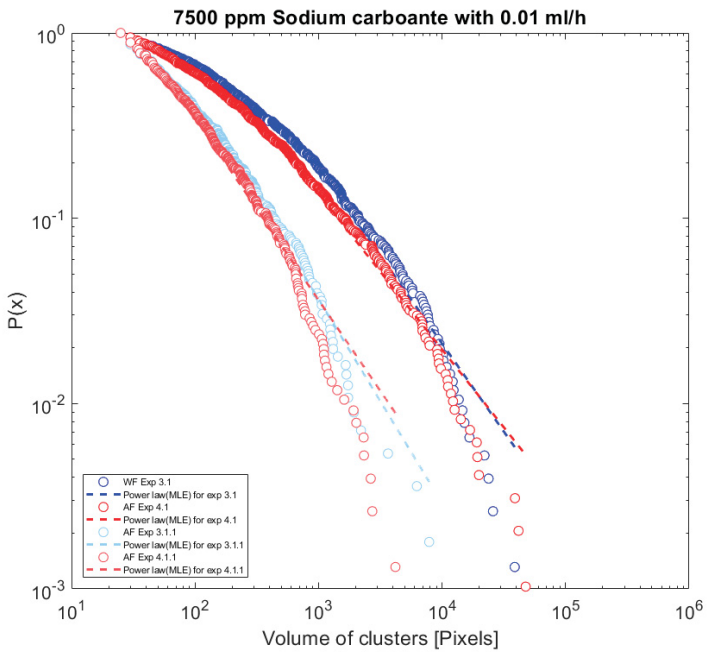
7500 ppm Sodium carboante with 0.01 ml/h
P(x)
WF Exp 3.1
Power law(MLE) for exp 3.1
AF Exp 4.1
Power law(MLE) for exp 4.1
AF Exp 3.1.1
Power law(MLE) for exp 3.1.1
AF Exp 4.1.1
Power law(MLE) for exp 4.1.1
Volume of clusters [Pixels]

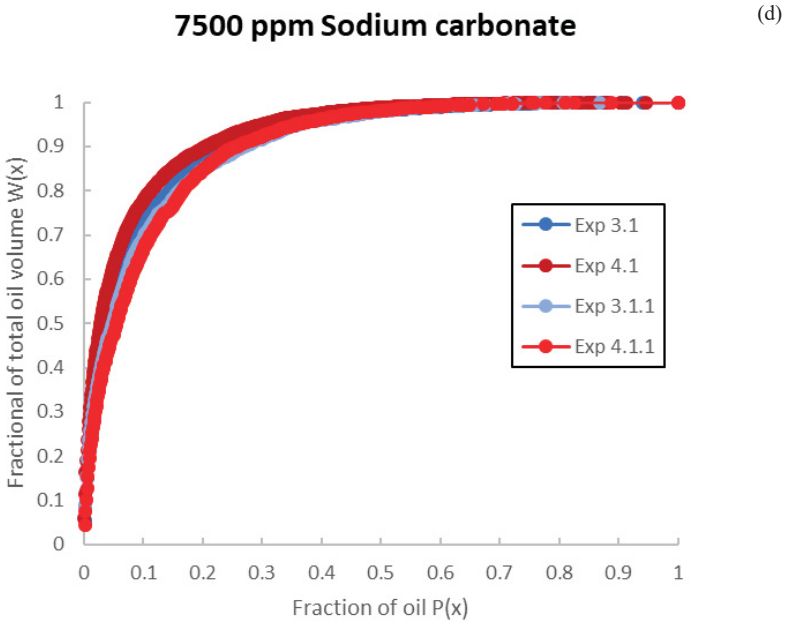

Figure 5-14- Statistical analyses for 7500 ppm Na_2CO_3 a) cluster size distribution for AF, b) cluster size distribution for WF and AF, c) Normalize distribution, d) Lorenz plot

Synthetic AF with 3000 and 7500 ppm Na_2CO_3 (Experiments 5 and 6)

Compared to water flooding with distilled water, synthetic water floods show a significant higher recovery. However, an alkaline solution with synthetic water did not result in considerable recovery (Figure 5-15). It should be mentioned that the IFT value for 3000 and 7500 ppm Na_2CO_3 solutions on basis of synthetic water are respectively 0.15 mN/m and 0.3 mN/m (Arnold, 2018), which are one order of magnitude higher than pure synthetic water.

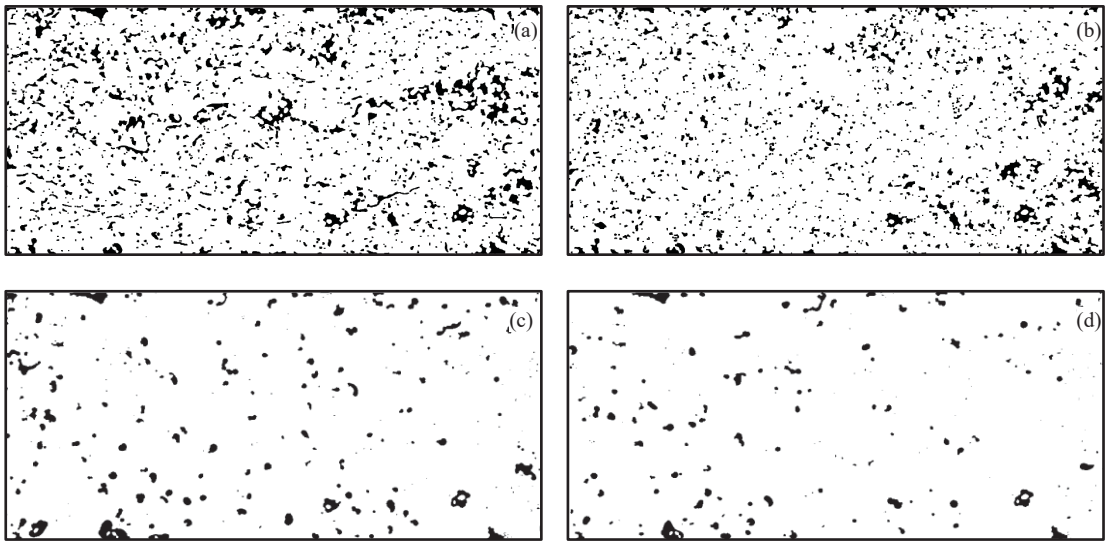

Figure 5-15- Synthetic flooding a) Experiment 5.1, b) Experiment 5.1.1, c) Experiment 6.1 d) Experiment 6.1.1

Even though the clusters break down as in the formerly discussed alkaline cases, cluster tends to remain in the porous medium which is indicated in the cluster size distribution in Figure 5-16-b; the power law exponent fitted to the cumulative distributions for water and alkaline flooding did not change, but shifts to smaller cluster sizes. Interestingly, the Lorenz curve shows the same behavior before and after alkaline flooding, but are different for the two synthetic water. Note that, no microemulsion was observed in synthetic floods.

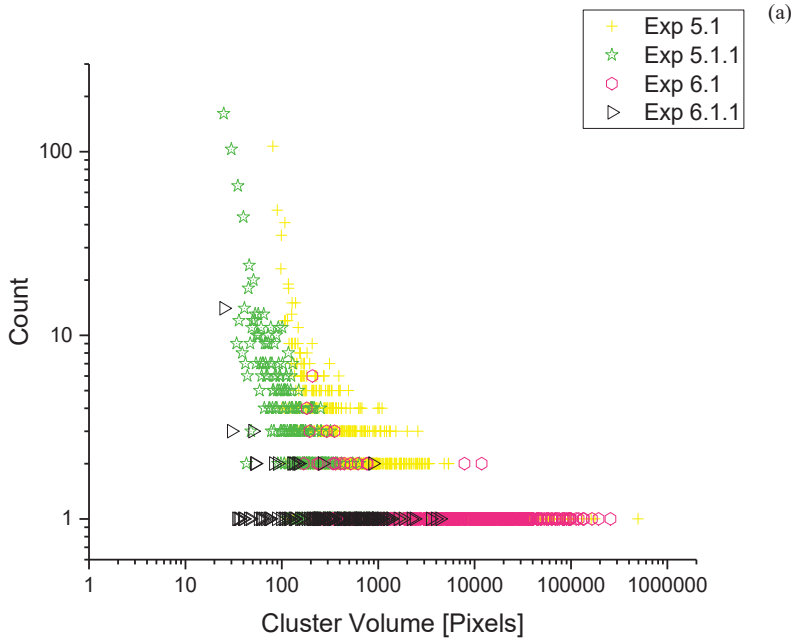

(a)

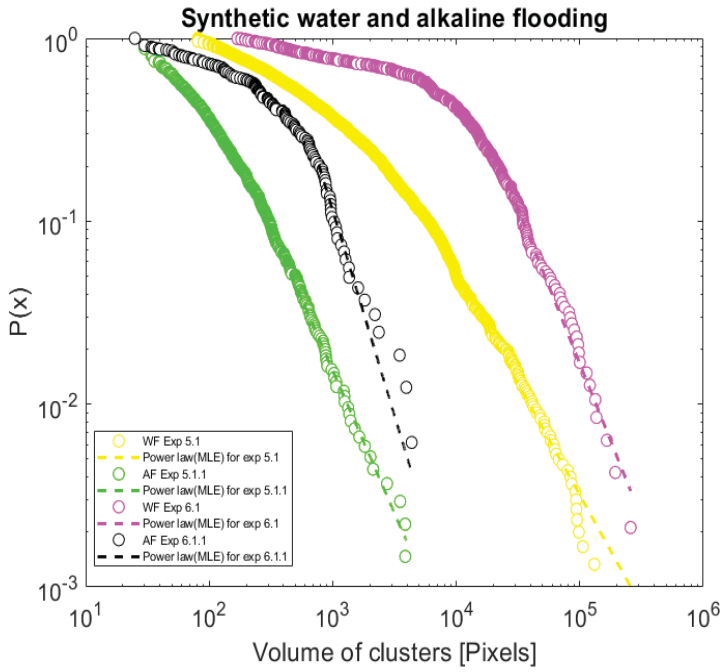

(b)

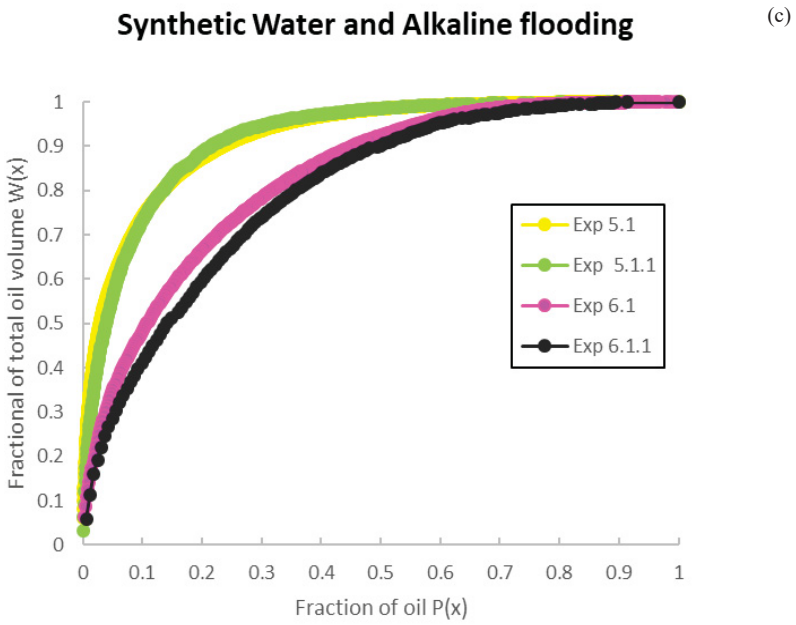

Figure 5-16- Statistical analyses for synthetic WF and AF, a) cluster size distribution for WF and AF, b) Normalize distribution, c) Lorenz plot

All the distilled alkaline flooding with 0.01 ml/h (Experiments 1-4 and 7)

In an additional experiment, 720 ppm NaOH was injected with the same injection rate. The results are compared in the following to the results discussed before for 3000 and 7500 ppm Na_2CO_3. Figure 5-17-a and Figure 5-17-b show the last stage of floods for 3000 ppm and 7500 ppm Na_2CO_3, respectively and is compared to the NaOH experiment in Figure 5-17-c. Additionally, the IFT value for both concentration of Na_2CO_3 is the same and give as 0.065 mN/m (Arnold, 2018). Note that microemulsion generation was observed for 7500 ppm Na_2CO_3 concentration in both, microfluidics and spinning drop (Arnold2018). Figure 5-18 shows that generated microemulsion is pinning the cluster on solid surfaces in micromodel.

Moreover, 3000 ppm Na_2CO_3 and 720 ppm NaOH show similar tertiary recovery factors, but different displacement processes are observed. In Na_2CO_3 flooding, residual oil is recovered from dead-end pores, while with NaOH, oil remains in dead-end pores.

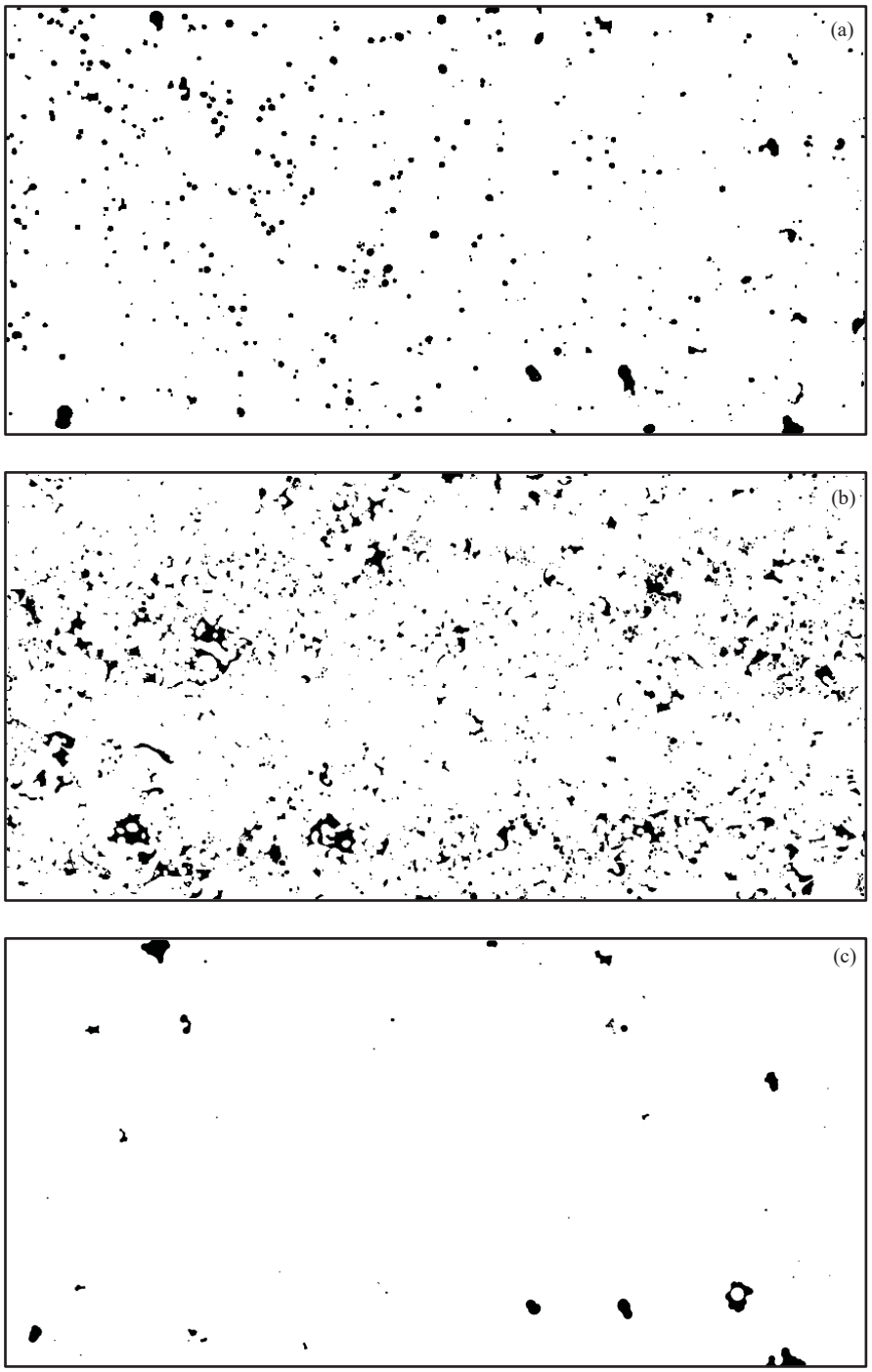

Figure 5-17- Process images of the final stage, a) Exp 2.1.1 (3000 ppm Na_2CO_3), b) Exp 4.1.1 (7500 ppm Na_2CO_3), c) Exp 7.1.1 (720 ppm NaOH)

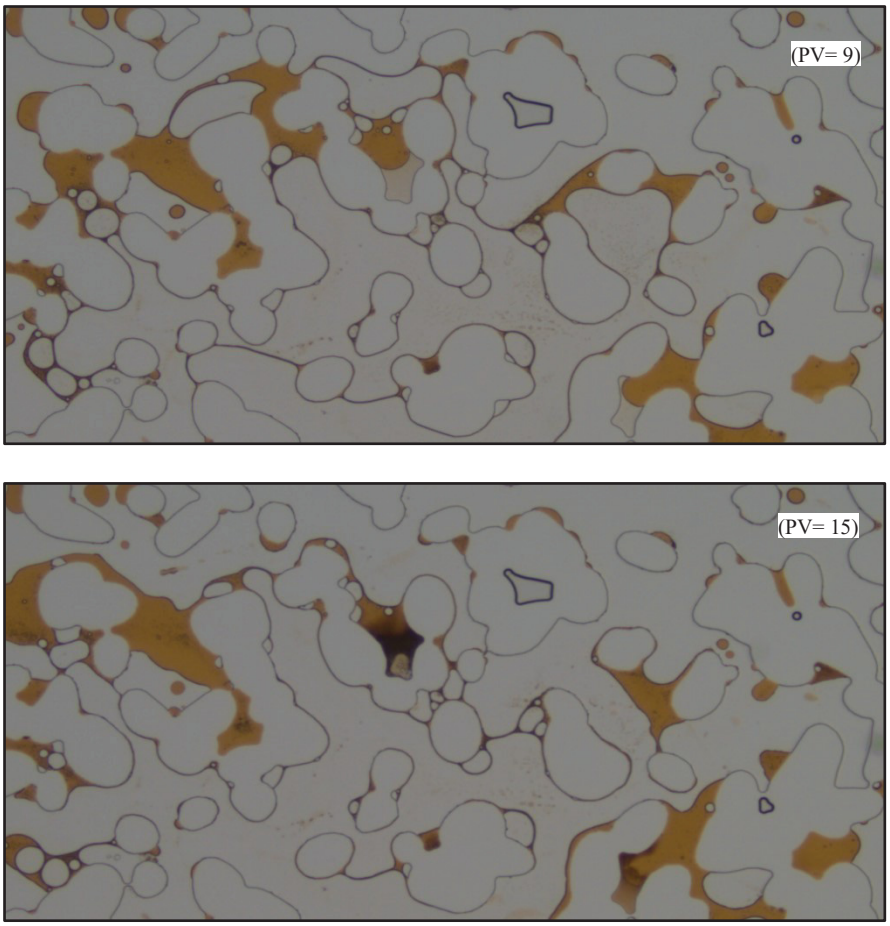

Figure 5-18- Pinned clusters due to microemulsion in 7500 ppm Na_2CO_3 in different pore volume

The microemulsion generation during 7500 ppm concentration was shown in Figure 5-19. After 15 pore volumes injection, the phase separation is observed.

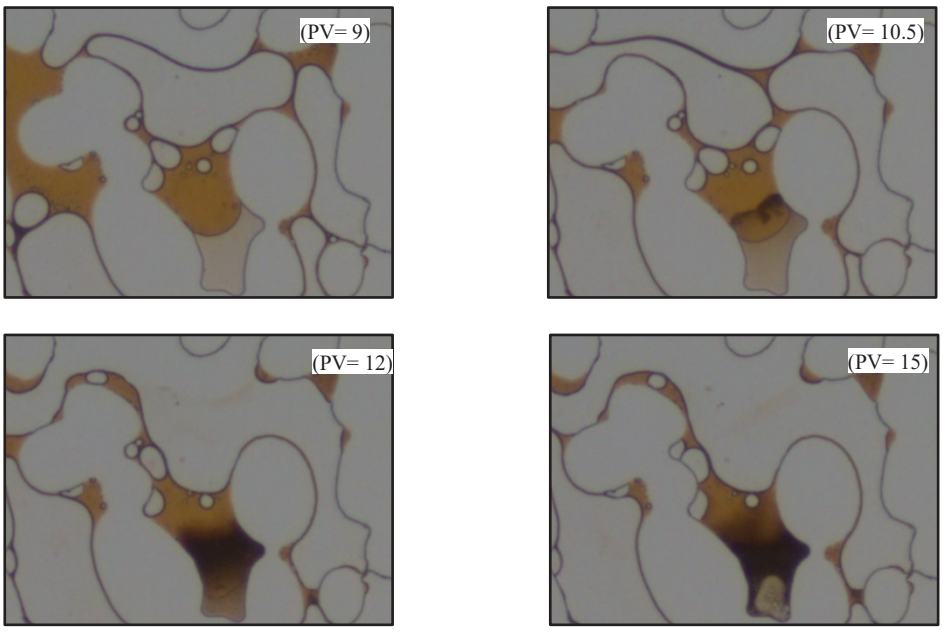

Figure 5-19- Microemulsion generation in 7500 ppm Na_2CO_3 flooding in different pore volume

Comparing the generated droplet's shape in micromodel with the spinning drop, the droplets in 3000 ppm Na_2CO_3 are separated and have regular distance from each other (Figure 5-20-a), while the droplets are attached together in 7500 ppm concentration (Figure 5-20-b).

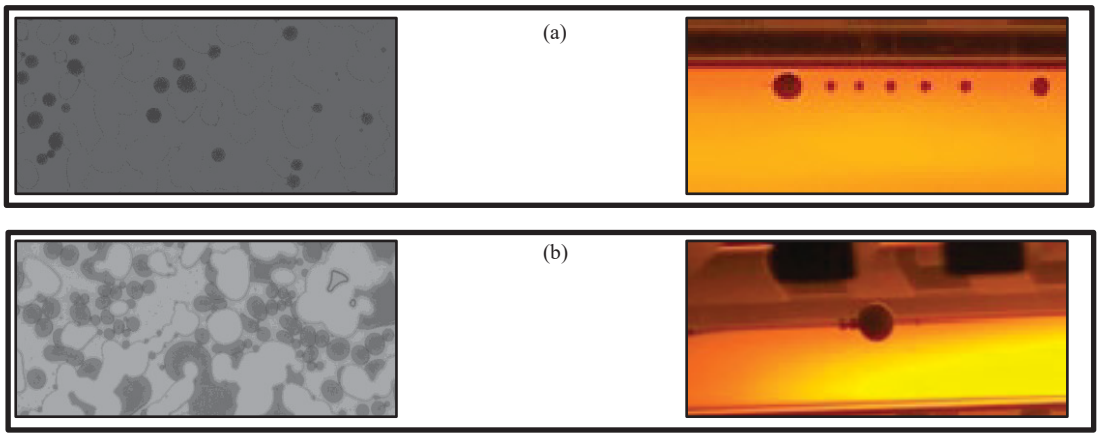

Figure 5-20- Images of droplets in micromodel and spinning drop of Na_2CO_3 a)3000 ppm, b) 7500 ppm

Comparing all the water flooding experiments with subsequent alkaline flooding at a single flow rate, it is observed that the cluster sizes after alkaline floods are smaller compared to prior water flooding (Figure 5-21-a). Moreover, Figure 5-21-b shows the water floods have a higher probability of the larger cluster volume compare to the alkaline flooding. Besides, the fitted power laws exponents in waterflooding have a similar trend. This similarity in a different way is also observed in the alkaline flooding, except experiment 7.1.1, where too little clusters of oil remained in the micromodel to make a reasonable statistic. In conclusion, this graph is demonstrated a significant fingerprint for identifying and discriminating water and alkaline flooding and their behavior. Additionally, a clear trend has been identified in the Lorenz plots, where alkaline flooding experiments generated more homogeneous cluster volume distribution than water floods (Figure 5-21-c).

(a)

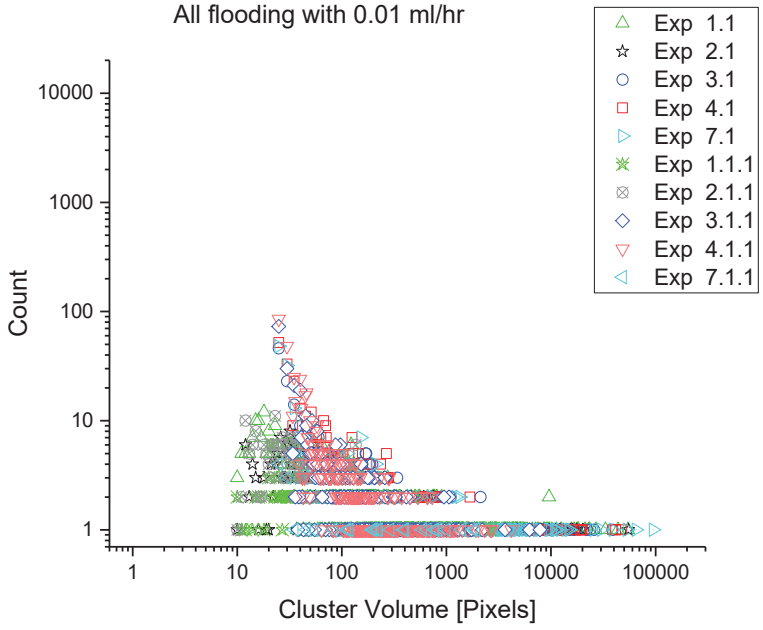
All flooding with 0.01 ml/hr
Exp 1.1
Exp 2.1
Exp 3.1
Exp 4.1
Exp 7.1
Exp 1.1.1
Exp 2.1.1
Exp 3.1.1
Exp 4.1.1
Exp 7.1.1
Count
10000
1000
100
10
1
1
10
100
1000
10000
100000
Cluster Volume [Pixels]

(b)

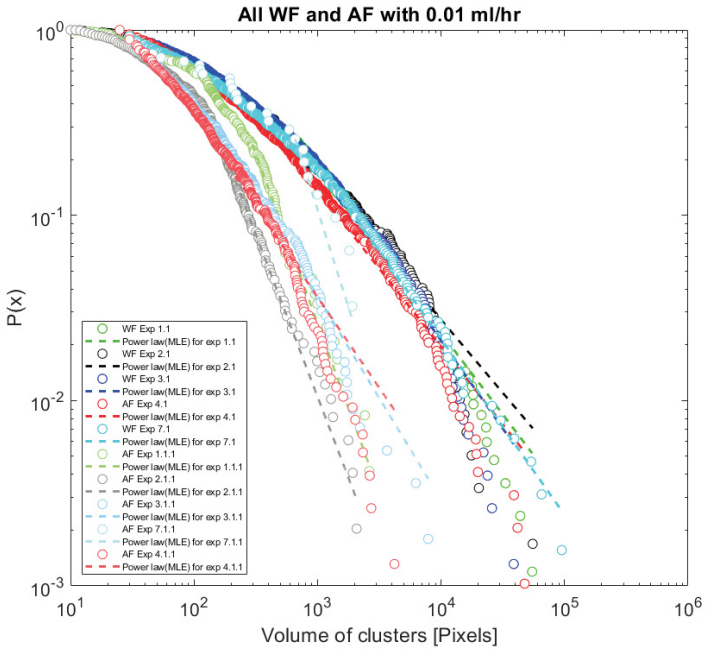
All WF and AF with 0.01 ml/hr
P(x)
Volume of clusters [Pixels]
WF Exp 1.1
Power law(MLE) for exp 1.1
WF Exp 2.1
Power law(MLE) for exp 2.1
WF Exp 3.1
Power law(MLE) for exp 3.1
AF Exp 4.1
Power law(MLE) for exp 4.1
WF Exp 7.1
Power law(MLE) for exp 7.1
AF Exp 1.1.1
Power law(MLE) for exp 1.1.1
AF Exp 2.1.1
Power law(MLE) for exp 2.1.1
AF Exp 3.1.1
Power law(MLE) for exp 3.1.1
AF Exp 7.1.1
Power law(MLE) for exp 7.1.1
AF Exp 4.1.1
Power law(MLE) for exp 4.1.1

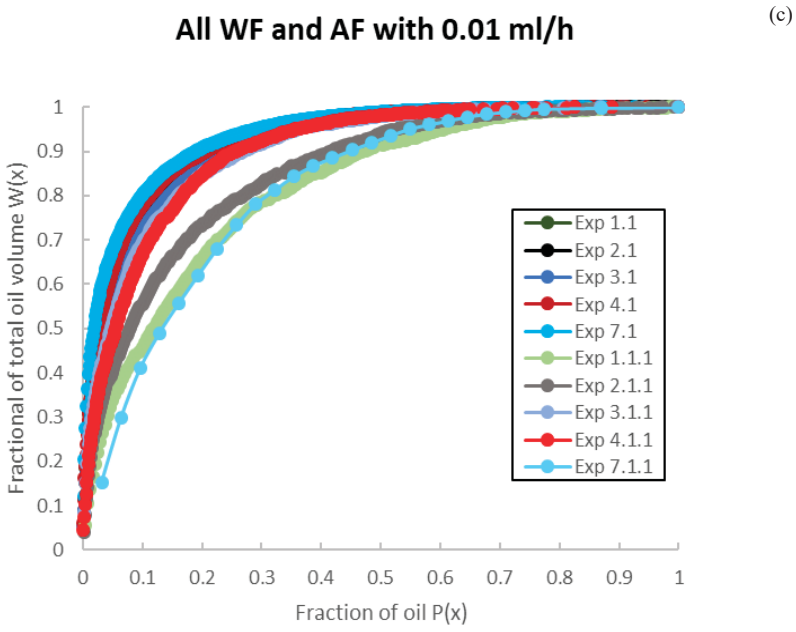

Figure 5-21- Statistical analyses for all flooding with 0.01 ml/h, a) cluster size distribution for WF and AF, b) Normalize distribution, c) Lorenz plot

5.2.3 Different injection rate in physical rock pattern (Experiments 7 and 9)

The comparison of water flooding using different injection rates results in a minor change in recovery factor which is about ~43%. However, with lower injection rate, the bypassing of oil or channeling is more likely to occur forming preferred pathways. In Figure 5-22-a, such pathways are visible in top and bottom of micromodel.

Nevertheless, the difference is more significant in alkaline flooding, where the recovery is lower for the lower injection rate. This performance can be described by the capillary number, where all the parameters are constant but the flow rate and hence the viscous force, where a higher flow rate means a higher capillary number. Therefore, the small droplets are remaining in the micromodel. In Figure 5-22-b, the small droplets are observed which are not recovered from the system in comparison to Figure 5-17-c, where most of the cluster are displaced from the porous domain.

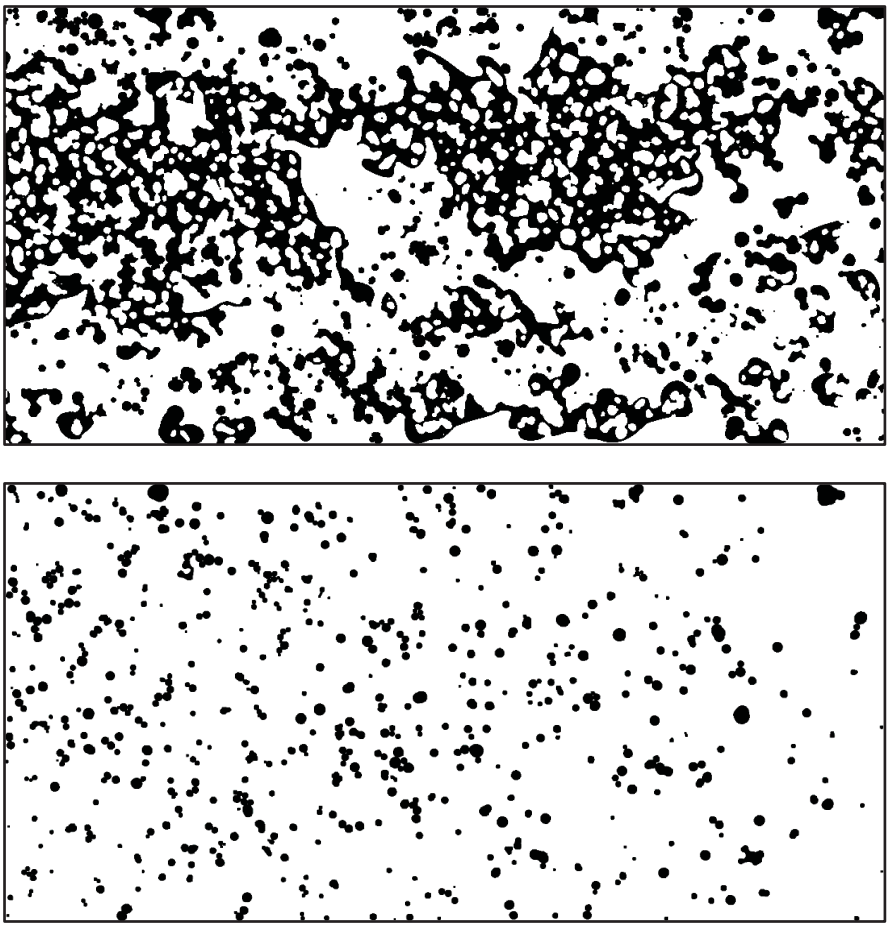

Figure 5-22- Last stage of flooding a) water, b) 720 ppm NaOH flooding

The cluster-volume size distribution illustrated that most of the small droplets are recovered from micromodel in the alkaline floods with higher injection rate (Experiment 7.1.1). In the case of lower injection rate (Experiment 9.1.1), the large clusters break into smaller clusters that mainly remain in the system (Figure 5-23-a). In Figure 5-23-b and Figure 5-23-c, similar trends for water and alkaline flooding were found, indicating that cluster size distribution is largely independent of flow rate.

(a)

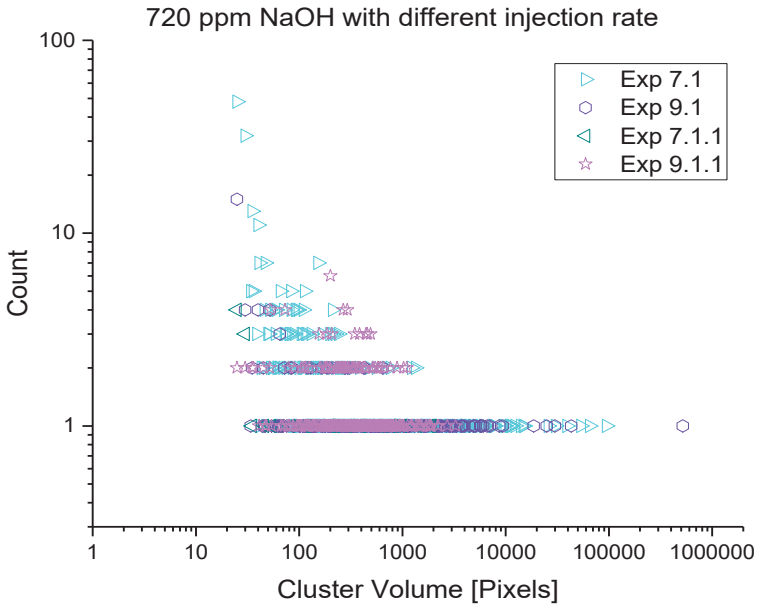
720 ppm NaOH with different injection rate
Exp 7.1
Exp 9.1
Exp 7.1.1
Exp 9.1.1
Count
Cluster Volume [Pixels]

(b)

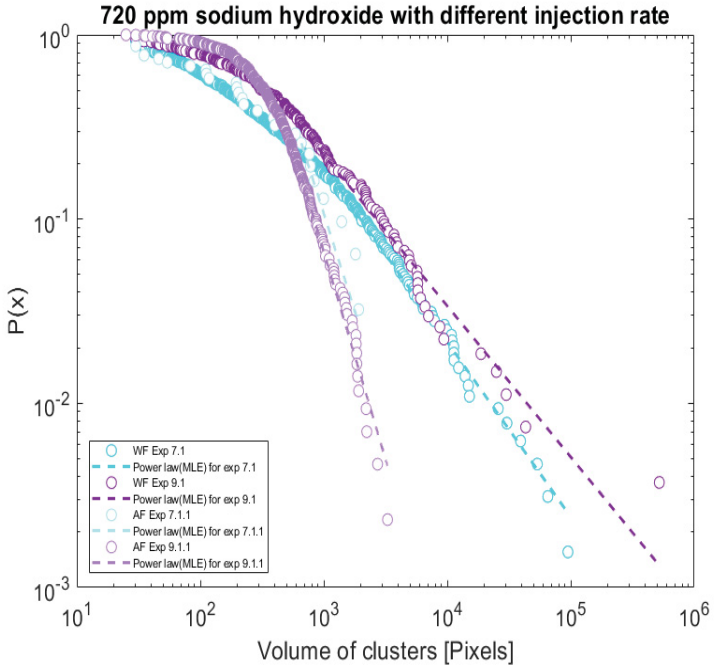
720 ppm sodium hydroxide with different injection rate
WF Exp 7.1
Power law(MLE) for exp 7.1
WF Exp 9.1
Power law(MLE) for exp 9.1
AF Exp 7.1.1
Power law(MLE) for exp 7.1.1
AF Exp 9.1.1
Power law(MLE) for exp 9.1.1
P(x)
Volume of clusters [Pixels]

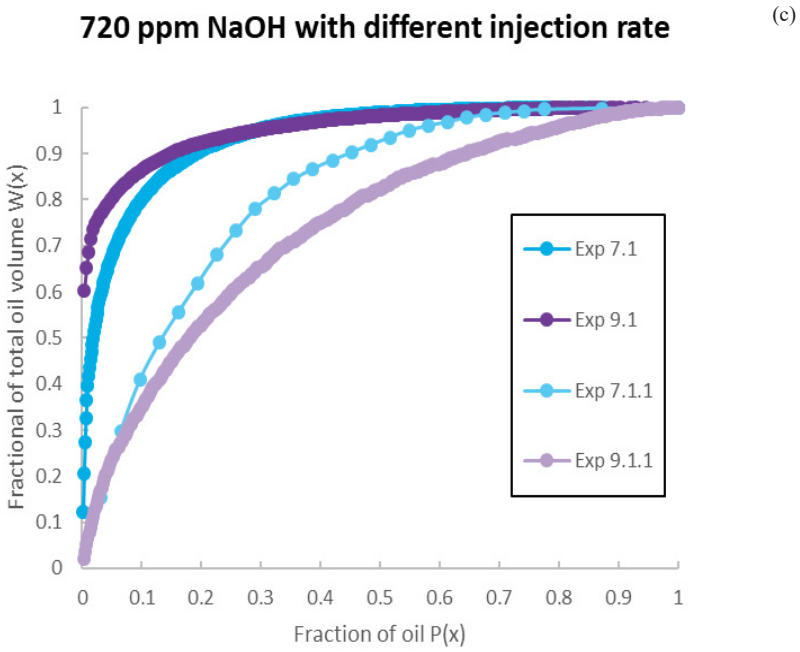

Figure 5-23- Statistical analyses for NaOH with different injection rate, a) cluster size distribution for WF and AF, b) Normalize distribution, c) Lorenz plot

5.2.4 Alkaline flooding with 0.001 ml/h rate in physical rock pattern

Results of alkaline flooding where microemulsion formation was observed are discussed and compared in the following.

720 ppm NaOH and 6000 ppm Na_2CO_3 (Experiments 9 and 12)

Comparing cluster sizes of experiment 9 (720 ppm NaOH) with experiment 12 (6000 ppm Na_2CO_3), were more abundant compared to experiment 12 (6000 ppm Na_2CO_3). This behavior is observed by comparing Figure 5-22-b and Figure 5-24. In both solutions, the microemulsion was formed. However, the microemulsion in 6000 ppm Na_2CO_3 was more visible during the experiments and reduced the oil production by pinning the cluster on the solid boundaries. Figure 5-25 shows the generated microemulsion in experiment 12 (6000 ppm Na_2CO_3).

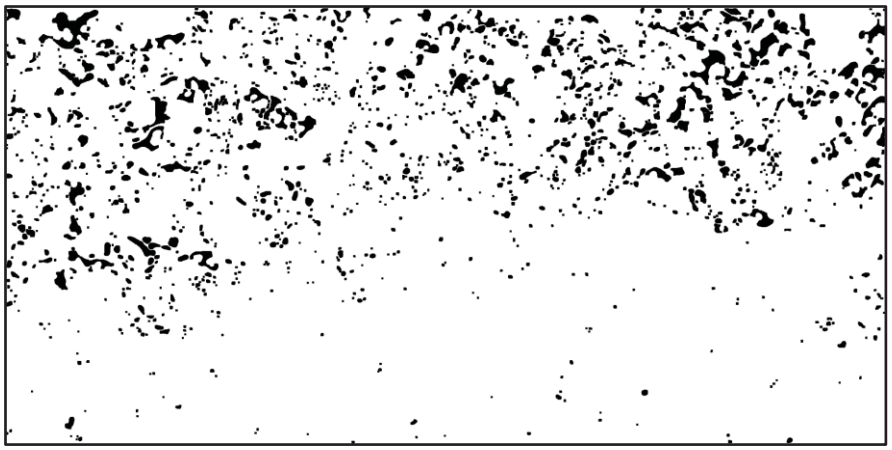

Figure 5-24- Last stage of experiment 12.1.1 (6000 ppm Na_2CO_3)

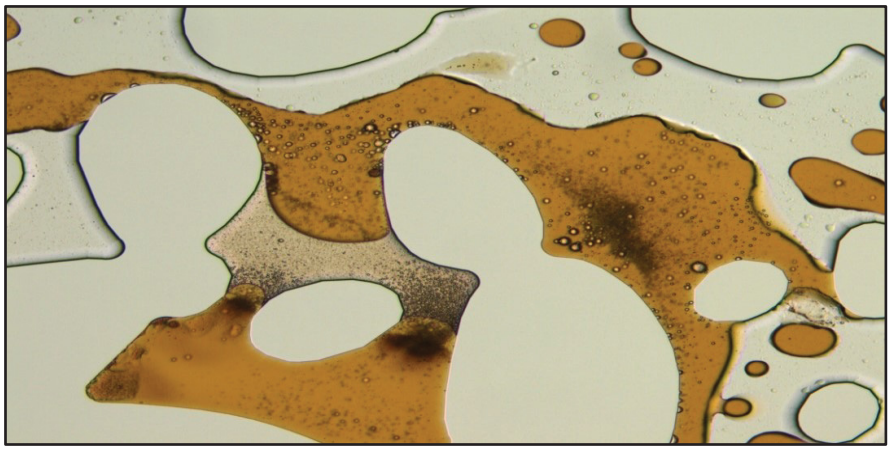

Figure 5-25- Microemulsion in experiment 12.1.1 (6000 ppm Na_2CO_3)

Comparing the water flooding experiments with subsequent alkaline flooding in lower injection rate, the similar trend as high injection rate is observed, where the cluster sizes after alkaline floods are smaller compared to prior water flooding (Figure 5-26-b). However, a different behavior was observed in the Lorenz plot for 6000 ppm Na_2CO_3 compared to 720 ppm NaOH (Figure 5-26-c), which is probably due to the microemulsion generation.

(a)

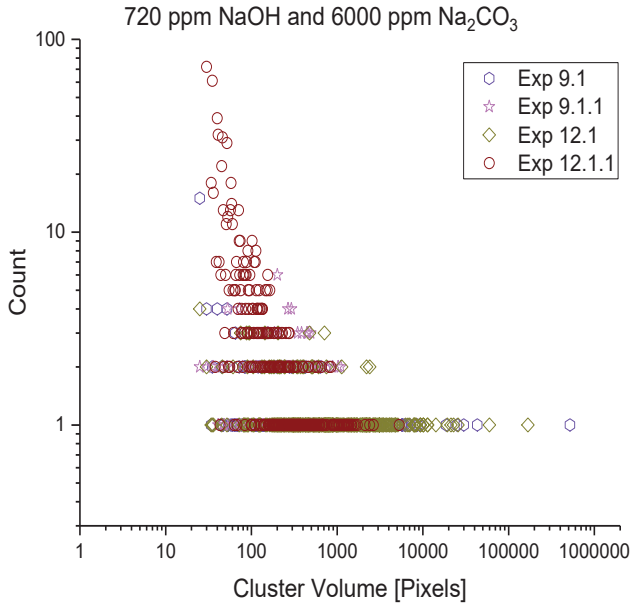
720 ppm NaOH and 6000 ppm Na_2CO_3
Exp 9.1
Exp 9.1.1
Exp 12.1
Exp 12.1.1
Count
Cluster Volume [Pixels]

(b)

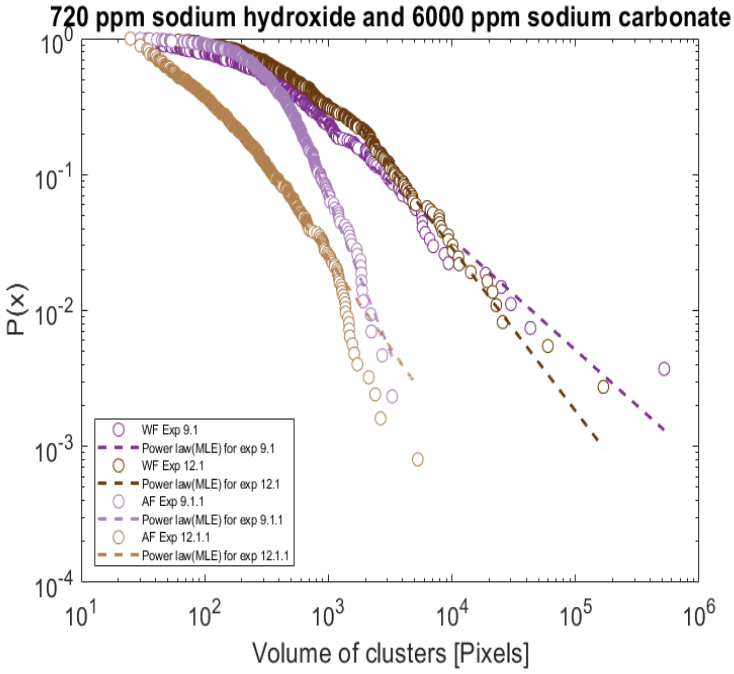
720 ppm sodium hydroxide and 6000 ppm sodium carbonate
WF Exp 9.1
Power law(MLE) for exp 9.1
WF Exp 12.1
Power law(MLE) for exp 12.1
AF Exp 9.1.1
Power law(MLE) for exp 9.1.1
AF Exp 12.1.1
Power law(MLE) for exp 12.1.1
P(x)
Volume of clusters [Pixels]

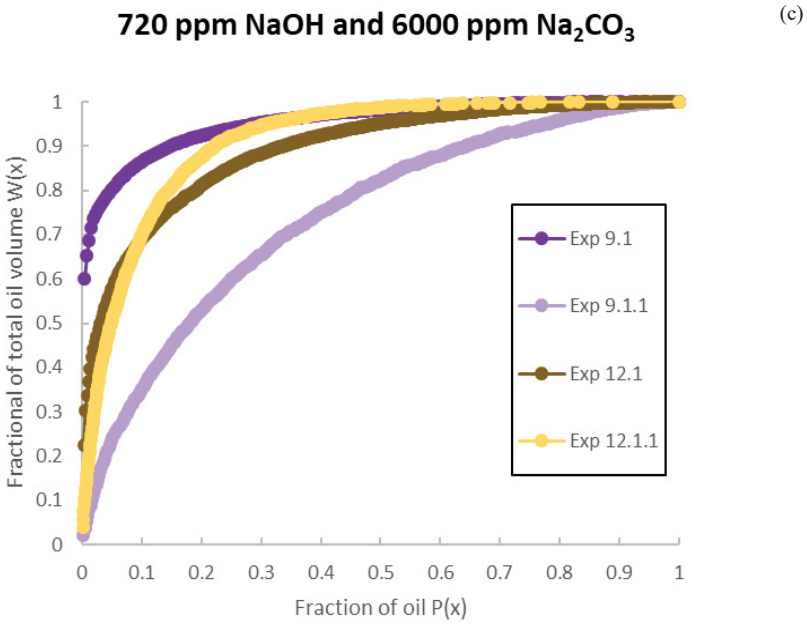

Figure 5-26- Statistical analyses for 6000 ppm Na2CO3 and 720 ppm NaOH, a) cluster size distribution for WF and AF, b) Normalize distribution, c) Lorenz plot

Experiments with microemulsion generation

Cluster size distribution is investigated by analyzing experiment 12.1.1 (6000 ppm Na_2CO_3) and 720 ppm sodium hydroxide in (Borji, 2017), where the enormous volume of microemulsion was observed. The interesting point is that in both experiments, the cluster size distribution is demonstrating the similar behavior (Figure 5-27).

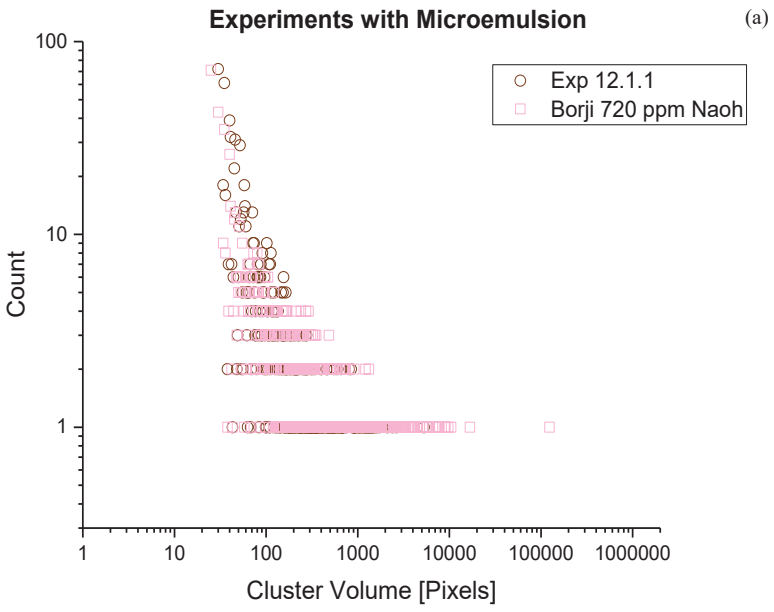

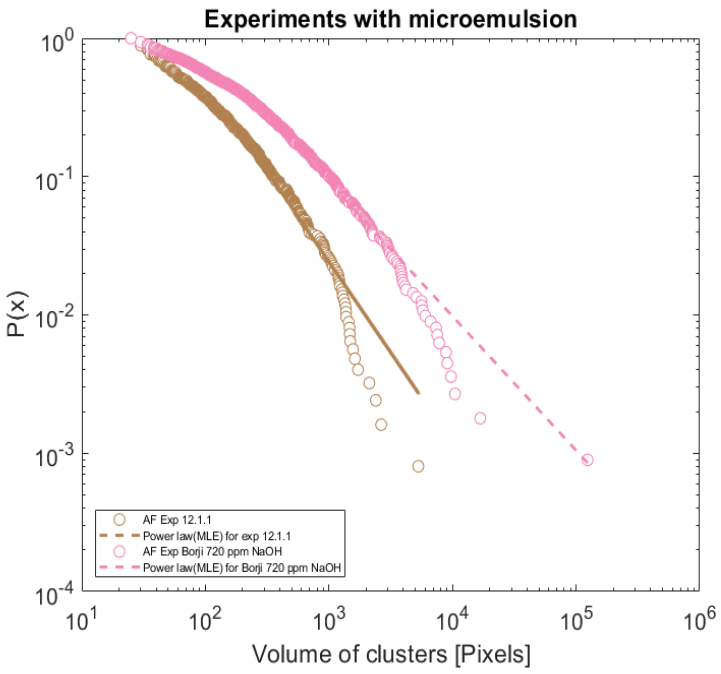

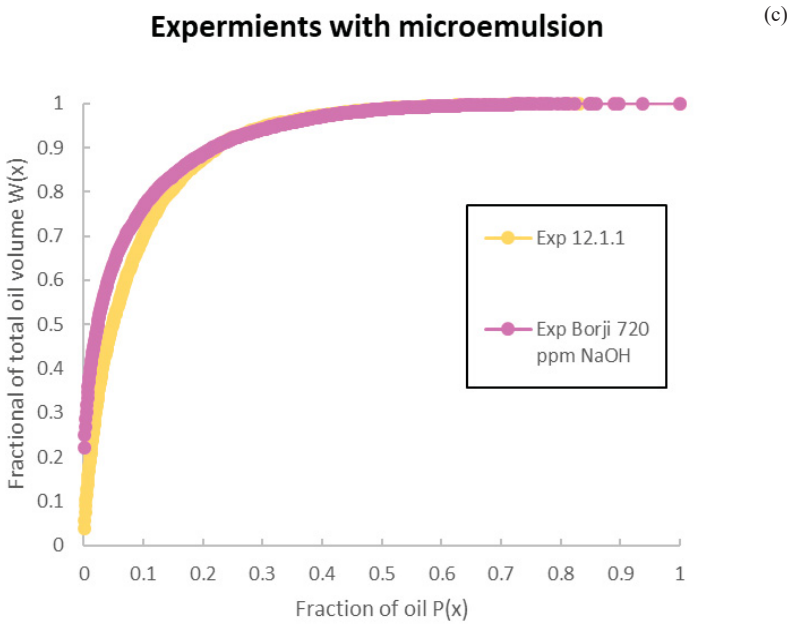

Figure 5-27- Statistical analyses for microemulsion generation, a) cluster size distribution for AF, b) Normalize distribution, c) Lorenz plot

5.2.5 Flooding in the uniform pattern

Waterflooding

The range of oil recovery for waterflooding in this pattern was between 40% to 50%. This variation might be due to channeling in the micromodel induced by displacement instabilities. Two channels in the upper and bottom part of the flooding domain were generated during water

flooding. Note that the main contrast between these floods was the displacement of oil through these channels. In more details, the secondary drainage occurs in this process, which is shown in Figure 5-28. The red square in Figure 5-28-a illustrates the spot, where the oil was swept after exposing to water after 0.4 pore volume of water injection. However, Figure 5-28-b shows that oil reinvaded water-flooded zones (secondary oil drainage) after 0.45 pore volume of water injection. In experiment 10.1 (Figure 5-29-a), besides the channeling in the top and bottom of the micromodel, oil in the middle of the micromodel was swept. In experiment 11.1 the channels are the main flow path, which is shown in Figure 5-29-b. In contrast, the channels were mostly blocked by oil after the secondary drainage in experiment 13.1, which is illustrated in Figure 5-29-c. Capillary fingering is considered as the displacement process for all of these floodings, where the logarithm of the capillary and mobility number is ~ -5 and 3, respectively. Based on Figure 2-5, they are located in capillary fingering domain of the diagram.

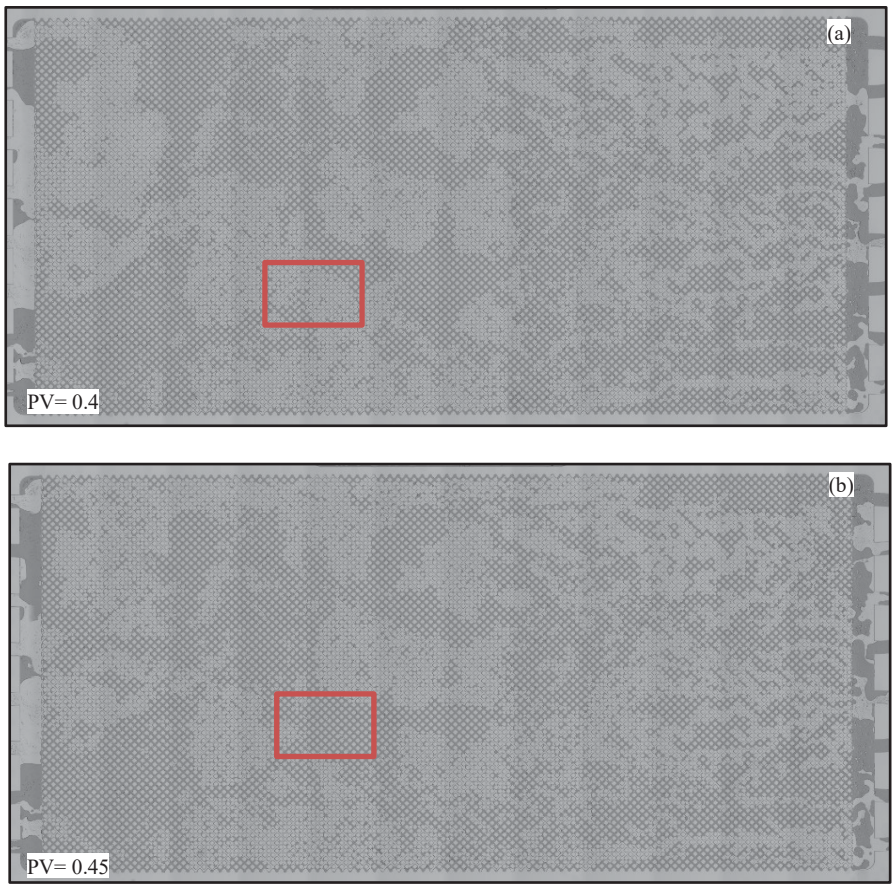

Figure 5-28- Secondary drainage in the uniform pattern

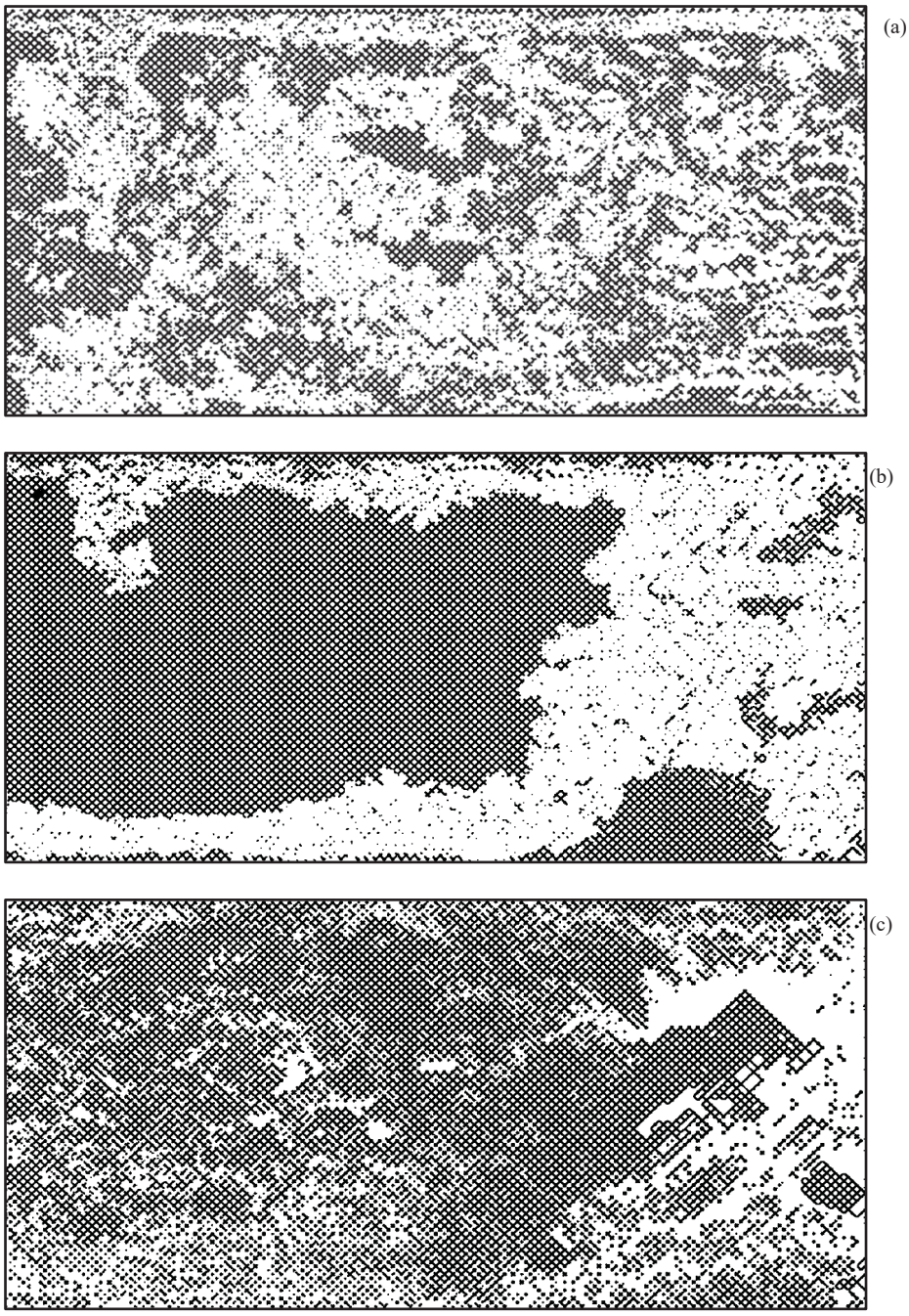

Figure 5-29- Binary image at the final stage of a) Experiment 10.1, b) Experiment 11.1, c) Experiment 13.1

Alkaline Flooding

In Figure 5-30-a, the alkaline flooding of experiment 10.1.1 (720 ppm NaOH) is shown. The results showed that oil production is mostly dependent on the pathways of the waterflood before the alkaline flooding. This is mainly due to the aqueous phase flowing in the initially created channels and the oil in between was mainly untouched. In Figure 5-30-b, the alkaline solution (950 ppm Na_2CO_3) swept the oil from inlet channels and changed oil saturation in the micromodel. However, the highest sweep efficiency was observed in experiment 13.1.1 (6000

ppm Na_2CO_3), where new channels were created during alkaline flooding (Figure 5-30-c). Hence, the quantitative comparison between different alkali solution in this pattern made not much sense. However, the capillary fingering is considered as a displacement process in these experiments same as waterflooding. The statistical analyses did not show any specific trend, which may have to do with the fact that the displacement is dominated by sweep effects and early breakthrough (Figure 5-31).

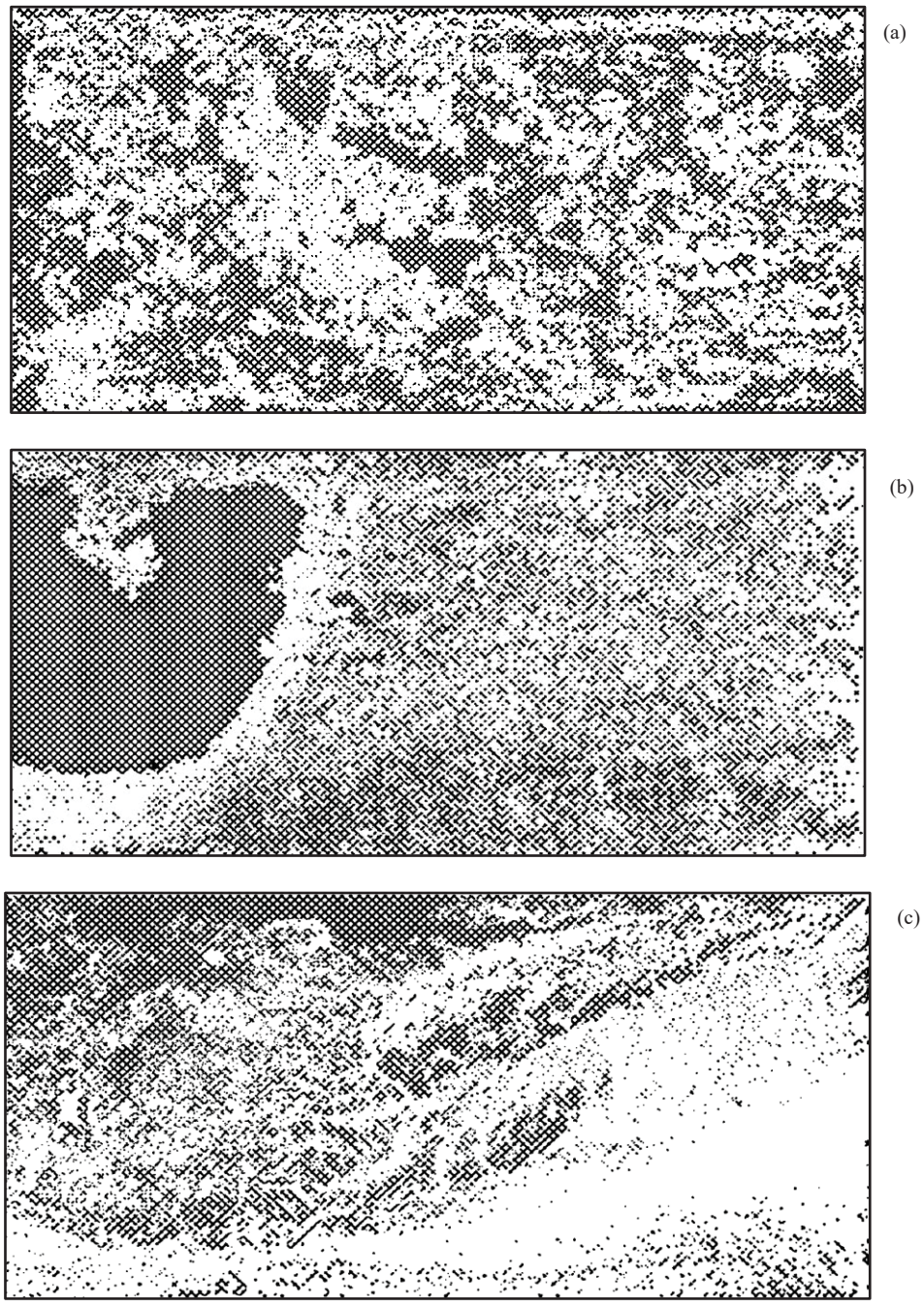

Figure 5-30- Binary image at the final stage of a) Experiment 10.1.1(720 ppm NaOH), b) Experiment 11.1.1(950 ppm Na_2CO_3), c) Experiment 13.1.1(6000 ppm Na_2CO_3)

(a)

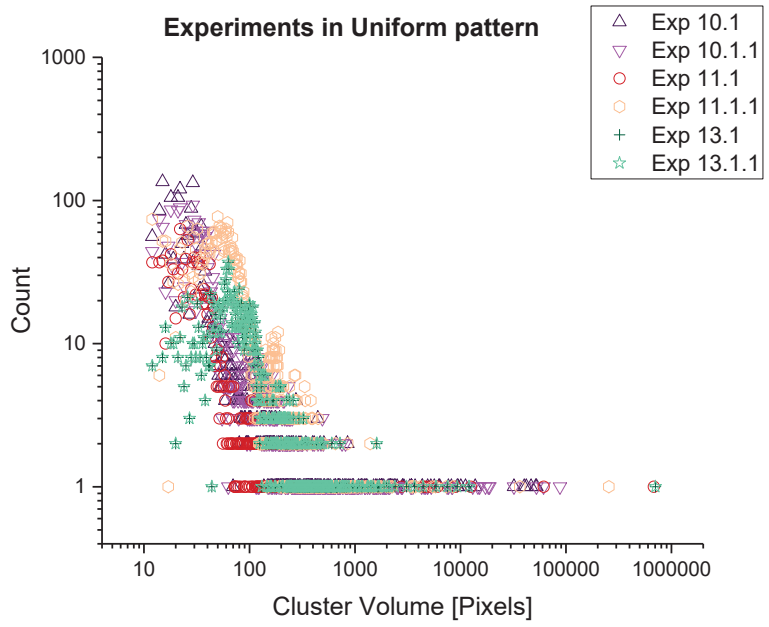
Experiments in Uniform pattern
Exp 10.1
Exp 10.1.1
Exp 11.1
Exp 11.1.1
Exp 13.1
Exp 13.1.1
Count
1000
100
10
1
10
100
1000
10000
100000
1000000
Cluster Volume [Pixels]

(b)

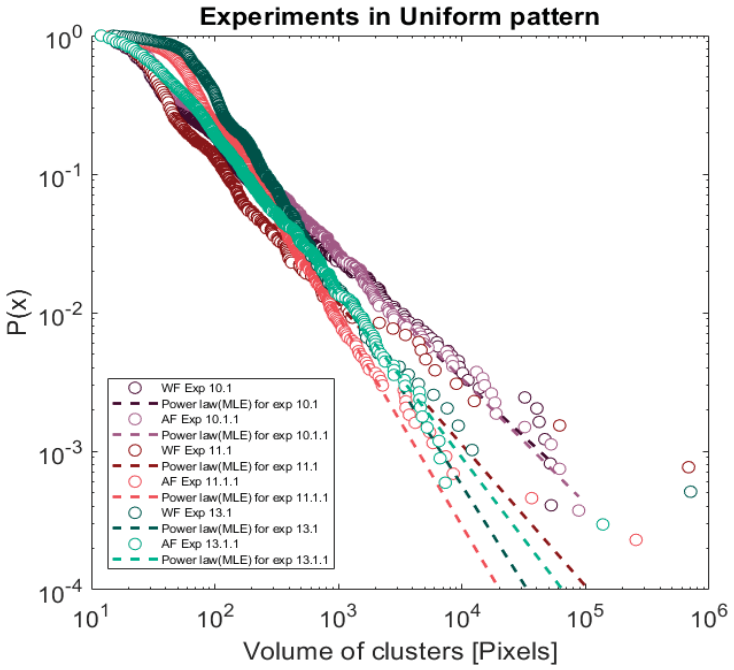
Experiments in Uniform pattern
P(x)
WF Exp 10.1
Power law(MLE) for exp 10.1
AF Exp 10.1.1
Power law(MLE) for exp 10.1.1
WF Exp 11.1
Power law(MLE) for exp 11.1
AF Exp 11.1.1
Power law(MLE) for exp 11.1.1
WF Exp 13.1
Power law(MLE) for exp 13.1
AF Exp 13.1.1
Power law(MLE) for exp 13.1.1
Volume of clusters [Pixels]

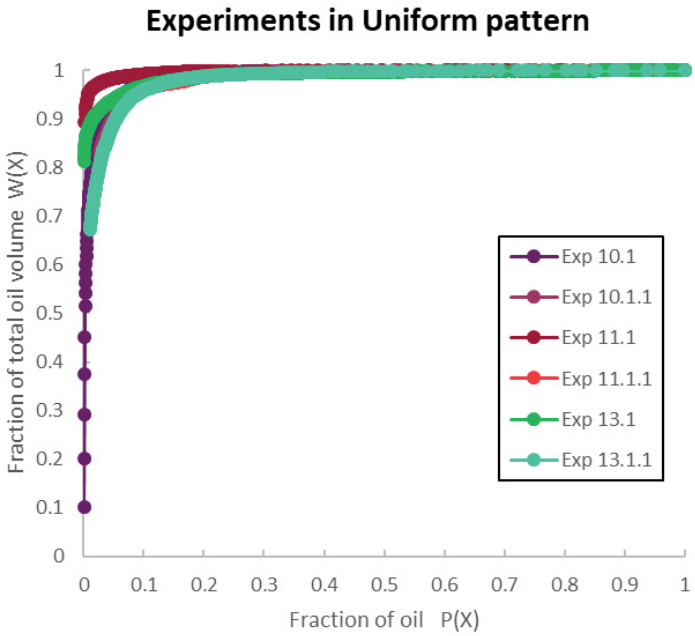

Figure 5-31- Statistical analyses for the uniform pattern, a) cluster size distribution for WF and AF, b) Normalize distribution, c) Lorenz plot

5.2.6 Comparison between two patterns

Ganglion dynamic and traffic flows droplets were observed in the uniform pattern experiments, while capillary forces disconnected the phases and formed small oil droplet (Figure 5-32-a). In addition, the capillary forces are lower in the physical rock pattern and the snap off was mainly observed due to the change of wetting conditions leading to a dispersion of the oil phase in small droplets (Figure 5-32-b).

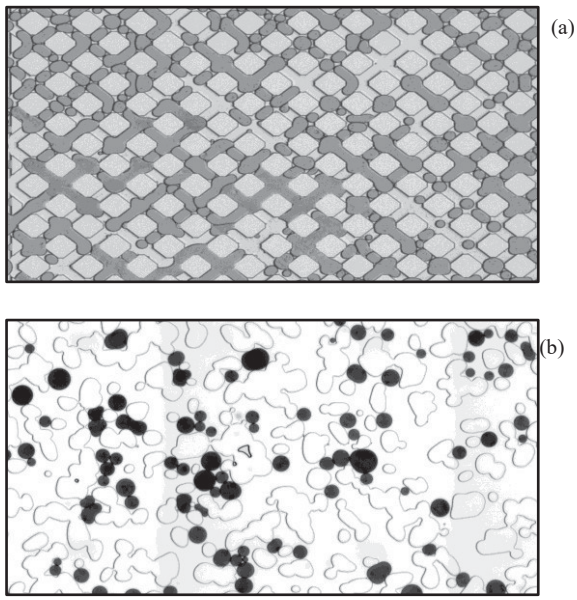

Figure 5-32- Flow pattern for a) Uniform, b) Physical rock

5.3 Capillary Desaturation curve

The capillary desaturation curve is plotted for the experiments by using the IFT value in Figure 5-33. As expected, water floods with lower injection rate (0.001 ml/h) have the least capillary number through all the experiments. In contrast, synthetic water flooding has the maximum capillary number. This graph illustrated that the critical capillary number is around 10^{-4}, where the residual oil saturation is reduced. Furthermore, the waterfloods mainly fall on the plateau region, where changing the injection rate (velocity) has a minor impact on the reduction of the residual oil saturation in the experiments.

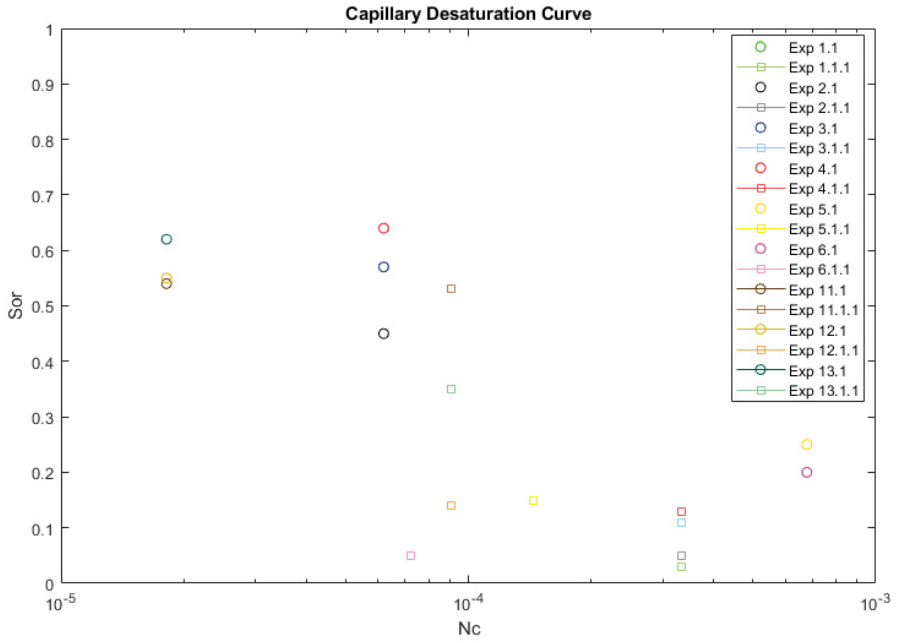

Figure 5-33- Capillary desaturation curve for the experiments

Chapter 6

Conclusion

6.1 Summary

In the frame of this thesis, alkaline flooding was investigated by using microfluidics. Several experiments have been performed under different conditions to study the effects of:

- Micromodel pattern types (physical rock and uniform)
- Alkaline type and concentration (Na_2CO_3 and NaOH)
- Water composition (pure water and synthetic water)
- Injection rate (0.01 ml/h and 0.001 ml/h).

The image processing shows that the recovery results have inconsistencies in the experiments due to the flooding domain which was not representing an elementary volume for two phase flow, which is a common problem in the area of pore-scale physics. Therefore, discrete frequency distributions, cumulative distributions and Lorenz plots, have been used to understand the performance of EOR processes by statistical means. Based on the obtained results statistical fingerprints have been found to describe the performance and mechanisms for water and alkaline flooding.

Upon visual observation, the synthetic water displaced a significant amount of oil compared to the distilled-water flood. In addition, the 3000 ppm Na_2CO_3 used in tertiary recovery, demonstrated an optimum displacement with respect to other concentration. This could be due to the reduced microemulsion generations. Among the two injection rates, the waterflooding showed the minor effect on oil recovery. However, in the case of 720 ppm NaOH flooding, the lower injection rate resulted in lower recovery due to lower viscous forces applied.

Additional experiments on the regular pore network showed that the displacement is dominated by capillary fingering. The displacement patterns stay in strong contrast to the displacement characteristics in the physical rock pattern.

6.2 Future Work

Further work for better understanding EOR chemical processes are recommended:

- Generation of capillary desaturation curve using a wide range of chemicals and injection rates
- Performing polymer-alkaline flooding in the uniform and non-uniform micromodel patterns to study the effect of capillary to viscous forces
- Studying the microemulsion generation and its impact on oil production
- Designing a new micromodel facilitating higher capillary contrast
- Investigating different displacement processes based on Lenormand plot's.

Chapter 7

References

A. Chatenever, J. Calhoun, 1952. Visual examinations of fluid behavior in porous media. *PETROLEUM TRANSACTIONS,* Volume 195, pp. 149-156.

A. Georgiadis, S. Berg, A. Makurat, G. Maitland, H. Ott, 2013. Pore-scale micro-computed-tomography imaging: Nonwetting-phase cluster-size. *PHYSICAL REVIEW,* 88(3).

A. Lucian, R. Hilfer, 1999. Trapping and mobilization of residual fluid during capillary desaturation in porous media. *PHYSICAL REVIEW E,* 59(6), p. 6819–6823.

Aaron Clauset, Cosma Rohilla Shalizi, M. E. J. Newman, 2009. Power-Law Distributions in. *Society for Industrial and Applied Mathematics,* Volume 51, pp. 661-703.

Anon., n.d. *Dmi8 Leica.* [Online] Available at: https://www.leica-microsystems.com/products/light-microscopes/inverted-microscopes/details/product/leica-dmi8/

Arnold, P., 2018. *Experimental investigation of interfacial tension for alkaline flooding,* s.l.: Montan University Leoben.

Borji, M., 2017. *Alkali-based Displacement Processes in Microfluidic Experiments: Application to the Matzen Oil Field,* s.l.: Montan University Leoben.

C. E. Cooke Jr., R. E. Williams, P. A. Kolodzie, 1974. Oil Recovery by Alkaline Waterfiooding. *PETROLEUM TECHNOLOGY,* pp. 1366-1374.

C. E. Cooke, J. R. E. W. P. A. K., 1974. Oil Recovery by Alkaline Waterfiooding. *SPE.*

C. Mattax, J.R. Kyte, 1962. Imbibition Oil Recovery from Fractured, Water-Drive Reservoir. *SPE,* 2(02), pp. 177-184.

Cheng JT, Giordano N, 2002. Fluid flow through nanometer-scale channels. *Physical Review,* p. 5.

Christophe Cottin, Hugues Bodiguel, Annie Colin, 2010. Drainage in two-dimensional porous media: From capillary fingering to viscous flow. *PHYSICAL REVIEW.*

Dullien, F. A., 1979. *Porous media fluid transport and pore structure.* s.l.:ACADEMIC PRESS.

E.F. deZabala, J. V. E. R. C. R., 1982. A Chemical Theory for Linear Alkaline Flooding. *SPE.*

Ehrlich R., Hasiba H.H., Raimondi P., 1974. Alkaline waterflooding for wettability alternation. *Petroleum Technology,* pp. 1335-1352.

Hu Guo, Ma Dou, Wang Hanqing, Fuyong Wang, Gu Yuanyuan, Zhaoyan Yu, Wang Yansheng, Yiqiang Li, 2017. Proper Use of Capillary Number in Chemical Flooding. *Hindawi Journal of Chemistry,* Volume 2017, p. 11.

ImageJ, 2017. *3D_Objects_Counter.* [Online] Available at: https://imagej.net/3D_Objects_Counter [Accessed 9 August 2018].

International Energy Agency, 2013. *IEA,* s.l.: International Energy Agency.

J. C. Melrose, C. F. Brandner, 1974. Role of Capillary Forces in Determining Microscopic Displacement Efficiency for Oil Recovery by Waterflooding. *The Journal of Canadian Petroleum,* pp. 54-62.

Jennings, H. Y., Jr., Johnson, C. E., Jr., and McAuliffe, C. D, 1974. Caustic Waterflooding Process for Heavy Oils. *Petroleum Technology,* pp. 1344-1352.

Johnson, C. E., 1976. Status of Caustic and Emulsion Methods. *PETROLEUM TECHNOLOGY,* pp. 85-92.

Lake, L. W., 1989. *Enhanced oil recovery.* s.l.:Prentice-Hall Inc., Englewood Cliffs.

Larry W. Lake, R. J. B. R. a. G. P., 2014. *Fundamentals of Enhanced Oil Recovery.* s.l.:Society of Petroleum Engineers.

Micronit, 2018. *Micronit Chipholder.* [Online] Available at: https://store.micronit.com/chipholders/fluidic-connect-4515-chipholder

Micronit, 2018. *Micronit EOR micromodel.* [Online] Available at: https://store.micronit.com/microfluidic-chips/enhanced-oil-recovery-chips/3-pack-eor-chips-physical-rock-network-443

Mohsen Yeganeh, Jessica Hegner, Eric Lewandowski, Aruna Mohan, Larry W. Lake, Dan Cherney, Arben Jusufi, Aditya Jaishankar , 2016. Capillary Desaturation Curve Fundamentals. *SPE ,* p. 14.

N. K. Karadimitriou and S. M. Hassanizadeh, 2012. A Review of Micromodels and Their Use in Two-Phase Flow Studies. *Vadose Zone,* Volume 11.

Nutting, P. G., 1925. Chemical Problems in the Water Driving of Petroleum from Oil Sands. *Industrial and Engineering Chemistry.*

O.R. Wagner, R.O. Leach, 1959. Improving Oil Displacement Efficiency by Wettability Adjustment. *Transactions of the AIME,* 216(1), pp. 65-72.

Ott, H., 2018. *Microfluidics for EOR Screening Application to Alkaline Flooding.* Copenhagen, EAGE.

Prosense, 2018. *NE 300 Syringe pump.* [Online] Available at: http://www.prosense.net/prosense/product-database/ne300-single-syringe-pump-just-infusion/2242

R. Lenormand, 1990. Liquids in porous media. *Journal of Physics: Condensed Matter,* Volume 2.

Riyaz Kharrat, A. R., 2017. *Practical Improved Hydrocarbon Recovery: An Industrial Guide Book for EOR and IOR.* s.l.:LAP LAMBERT Academic Publishing.

Roland Lenormand, Cesar Zarcone, 1985. Invasion Percolation in an Etched Network: Measurement of a Fractal Dimension. *Physical Review,* pp. 2226-2230.

Ryan T. Armstrong, Apostolos Georgiadis, Holger Ott, Denis Klemin, Steffen Berg, 2014. Critical capillary number: Desaturation studied with fast X-ray. *GEOPHYSICAL RESEARCH LETTERS,* Volume 41, pp. 50-60.

S. Kokal, A. A.-K., 2010. *Enhanced oil recovery: challenges & opportunities,* s.l.: World Petroleum Council.

Shao-Yiu Hsu, Zhong-Yao Zhang, Chia-Wen Tsao, 2017. Thermoplastic Micromodel Investigation of Two-Phase Flows in a Fractured Porous Medium. *Micromachines.*

Sheng, J. J., 2011. *Modern Chemical Enhanced Oil Recovery.* s.l.:Gulf Professional Publishing.

Sheng, J. J., 2013. *Enhanced Oil Recovery Field Case Studies.* s.l.:Gulf Professional Publishing.

Sheng, J. J., 2015. Status of Alkaline Flooding Technology. *Petroleum Engineering & Technology,* Volume 5, pp. 44-50.

Squires, F., 1917. *Recovery of oil from oil-sands.* United States of America, Patent No. 1238355A.

Subkow, P., 1942. *Process for the removal of bitumen from bituminous deposits.* United States of America, Patent No. 2288857.

Y. Alzahid, P. MOstaghimi, M. Ebrahimi Warkiani, R T. Armstrong, 2017. Alkaline Surfactant Polymer Flooding: What happens at the pore scale. *SPE,* p. 17.

Yi-Feng Chen, Shu Fang, Dong-Sheng Wu, Ran Hu, 2017. Visualizing and quantifying the crossover from capillary fingering to viscous fingering in a rough fracture. *Water Resources Research,* 53(9), pp. 7756-7772.